1   **Ultramafic clasts from the South Chamorro serpentine mud volcano reveal a**

2   **polyphase serpentinization history of the Mariana forearc mantle**

3

4   **Wolf-Achim Kahl[a,*], Niels Jöns[a,b], Wolfgang Bach[a], Frieder Klein[c], Jeffrey C. Alt[d]**

5   [a] Department of Geosciences, University of Bremen, Klagenfurter Straße (GEO), D-

6   28359 Bremen, Germany

7   [b] Institut für Geologie, Mineralogie und Geophysik, Ruhr Universität Bochum, D-

8   44780 Bochum, Germany

9   [c] Department of Marine Chemistry and Geochemistry, Woods Hole Oceanographic

10   Institution, Woods Hole, MA, 02543, USA

11   [d] Dept. Earth and Environmental Sciences, The University of Michigan, Ann Arbor, MI

12   48109 USA

13   *Corresponding author: E-mail address: wakahl@uni-bremen.de

14

15

16   ABSTRACT

17   Serpentine seamounts located on the outer half of the pervasively fractured Mariana

18   forearc provide an excellent window into the forearc devolatilization processes, which

19   can strongly influence the cycling of volatiles and trace elements in subduction

20   zones. Serpentinized ultramafic clasts recovered from an active mud volcano in the

21   Mariana forearc reveal microstructures, mineral assemblages and compositions that

22   are indicative of a complex polyphase alteration history. Petrologic phase relations

23   and oxygen isotopes suggest that ultramafic clasts were serpentinized at

24   temperatures below 200 °C. Several successive serpentinization events represented

25   by different vein generations with distinct trace element contents can be recognized.

26   Measured Rb/Cs ratios are fairly uniform ranging between 1 and 10, which is

27   consistent with Cs mobilization from sediments at lower temperatures and lends

28   further credence to the low-temperature conditions proposed in models of the

29 thermal structure in forearc settings. Late veins show lower fluid mobile element

30 (FME) concentrations than early veins, suggesting a deacreasing influence of fluid

31 discharge from sediments on the composition of the serpentinizing fluids. The

32 continuous microfabric and mineral chemical evolution observed in the ultramafic

33 clasts may have implications as to the origin and nature of the serpentinizing fluids.

34 We hypothesize that opal and smectite dehydration produce quartz-saturated fluids

35 with high FME contents and Rb/Cs between 1 and 4 that cause the early pervasive

36 serpentinization. The partially serpentinized material may then be eroded from the

37 basal plane of the suprasubduction mantle wedge. Serpentinization continued but the

38 interacting fluids did not carry the slab-flux signature, either because FME were no

39 longer released from the slab, or due to an en route loss of FMEs. Late chrysotile

40 veins that document the increased access of fluids in a now fluid-dominated regime

41 are characterized by reduced trace element contents with a slightly increased Rb/Cs

42 ratio near 10. This lack of geochemical slab signatures consistently displayed in all

43 late serpentinization stages may indicate that the slab-derived fluids have been

44 completely reset (i.e. the FME excesses were removed) by continued water-rock

45 reaction within the subduction channel. The final stage of diapiric rise of matrix and

46 clasts in the conduits is characterized by brucite-dominated alteration of the clasts

47 from the clast rim inward (independent of the intra-clast fabric relations), which

48 corresponds to re-equilibration with alkaline, low-silica activity fluids in the rising mud.

49

52

53

1. Introduction

Subduction zones are sites of intense mass transfer between the subducting plate and the Earth's mantle. The incoming slab of oceanic lithosphere (sediments, as well as variably altered mafic and ultramafic rocks) releases a generally high but variable fluid flux (Bebout 2007). As a consequence of rheological contrasts between the juxtaposed rock-types, shearing and metasomatism evolve a complex mélange zone atop the slab (i.e., the subduction channel) where rocks and fluids are extensively modified (Cloos and Shreve 1988a, 1988b). The inventory of slab lithologies and the thermal structure determine where fluids leave the slab and where they enter the subduction channel (Schmidt and Poli, 1998; Reynard, 2013; Spandler and Pirard, 2013). In particular, the flux of fluids is affected by the local setting, e.g., the slab dipping angle and the presence, or absence, of an accretionary sedimentary wedge. During subduction, the downgoing slab progressively releases water (Hyndman and Peacock, 2006): at shallow depths by porosity compaction and dehydration reactions of sediments, at intermediate depths by dehydration of sediments and altered oceanic crust, and, at greater depths, by continued dehydration of oceanic crust and deserpentinization of the subducting lithospheric mantle (Schmidt and Poli, 1998; Rüpke et al., 2002, 2004). The geochemical signature of the fluids' source lithologies is recorded by fluids and rocks affected by subduction zone processes: fore arc springs, metasomatized melange material, serpentinized mantle peridotites, and arc volcanism inherit the distinctive trace element contents of the reacting fluids (Parkinson and Pearce, 1998; Fryer et al., 1999; Mottl et al., 2003, 2004; Savov et al., 2005a; Hulme et al., 2010).

Mud volcanoes are a characteristic feature of the forearc of the Mariana subduction zone system (Fryer et al., 1985; 1999; 2000). Located along the outer half of the

81   deeply fractured Mariana forearc, diapiric mud volcanism has formed large edifices

82   from extrusion of blueschist and serpentine mud, up to 50 km in diameter and up to 2

83   km high (Fryer et al., 1990, 1999; Oakley et al., 2007). Systematic studies of pore

84   waters and vent fluid compositions suggest that the fluids fueling the serpentine mud

85   volcanoes are released from breakdown of hydrous phases in the subducting slab.

86   Most noticeably, these fluids have lower chloride, Mg, Ca, Sr, Li, and Si

87   concentrations, and higher pH, alkalinity, K, Na, Rb, Cs and Ba contents than

88   seawater, indicating slab dehydration and water-rock interactions in the conduits

89   feeding the mud volcanoes (Mottl, 1992; Benton et al., 2001; Mottl et al., 2003, 2004;

90   Wheat et al., 2008; Hulme et al., 2010). The occurrence of blueschist fragments in

91   the mud and rare metabasic clasts in the near-trench forearc region may indicate the

92   involvement of upward migrating fluids and melange material in the subduction

93   channel from deeper parts of the slab-mantle interface (e.g., Bebout, 2007).

94   However, geobarometry on metabasite schists from South Chamorro Seamount

95   (Fryer et al., 2006; 250-300 °C at a pressure of ~0.4-0.50 GPa, ~12-15 km) and

96   Conical Seamount (Maekawa et al., 1993; temperatures of ~175-250 °C and

97   pressures of 0.5-0.65 GPa, ~15-19.5 km) indicate their origin in depths slightly above

98   the base of the feeding conduits. Therefore, the erupted clast and mud materials

99   record changes in the composition of the slab-sourced fluids, progressively released

100   and accumulated in shallow and intermediate depths during subduction.

101

102   Trace element bulk rock compositions of serpentinized ultramafic clasts and

103   serpentine mud have been used to gain deeper insights into the composition of the

104   serpentinized forearc mantle (Savov et al., 2007; Deschamps et al., 2011), and to

105   deduce potential parent rocks of the serpentinizing fluids (e.g., Hulme et al., 2010).

106   At South Chamorro seamount, Ocean Drilling Program Leg 195 drilled Site 1200,

107   where ultramafic clasts occur within the mud matrix (Straub and Layne, 2003;

108   D'Antonio and Kristensen, 2004; Fryer and Salisbury 2006). These clasts record a

109 complex serpentinization history and provide an excellent window into the prevailing

110 fluid-rock interactions at, and above, the interface between the mantle wedge and the

111 subducting lithosphere. Moreover, the microfabrics of the highly serpentinized

112 harzburgite and dunite clasts exhibit evidence for multiple fracturing events in the

113 forearc mantle.

114

115 Here, we present a detailed investigation of trace element contents of the individual,

116 successive serpentine generations and the primary mantle minerals. As many of

117 these clasts have preserved domains representing early-stage serpentinization, we

118 can reconstruct much of the history of fluid-rock reaction in the Mariana forearc and

119 identify potential sources of the serpentinizing fluids.

120

121

122 **2. Setting and samples**

123

124 *South Chamorro Seamount*

125 Site 1200 is located on a knoll at the summit of south Chamorro Seamount in a water

126 depth of 2930 m (Salisbury et al., 2002). Hole A was drilled with a rotary core barrel

127 to a depth of 147.2 meters below seafloor (mbsf) and recovered mainly serpentinized

128 ultramafic clasts and minor amounts of the mud matrix. South Chamorro Seamount

129 (Fig. 1A) is one out of two dozen active mud volcanoes of the Mariana forearc,

130 located 85 km west the trench where the Mesozoic Pacific Plate is being subducted

131 west-northwestward beneath the West Philippine Plate (Fryer et al., 1990; Fig. 1B).

132 The serpentine mud volcano was drilled in 2000 at Site 1200 of the Ocean Drilling

133 Program (ODP) during Leg 195. Estimates of the slab depth beneath Site 1200

134 range between 26 km (Fryer, 1996; 1999) and 20 km (Oakley et al., 2005, 2007;

135 Fryer and Salisbury 2006). The seamount is composed of unconsolidated flows of

136 serpentine and blueschist mud with clasts of serpentinized mantle peridotite and

137 minor blueschist fragments (Fryer and Fryer, 1987; Fryer, 1996; Salisbury et al.,

138 2002; Fryer et al., 2006). The mudflow matrix consists of c. 90 % serpentine, as clay-

139 to silt-sized lizardite, chrysotile and minor antigorite. Accessory minerals of the

140 mudflow matrix include brucite, talc, mixed-layer smectite/illite clays, chlorite, relict

141 grains of primary silicates and Cr-spinel, amphibole and garnet. The sizes of clasts

142 recovered from Site 1200 vary from a few mm to >1 m in diameter. The clasts

143 represent lithologies from both the subducting plate and the suprasubduction-zone

144 mantle. In Hole 1200A, the peridotite clasts are predominantly harzburgites and

145 minor dunites. Serpentinization is extensive and ranges between ~40 % and 100 %

146 with an average alteration of 95 % for harzburgites and 75 % for dunites (D'Antonio

147 and Kristensen, 2004).

148 In this study, nine samples from the marginal parts of highly serpentinized clasts of

149 harzburgite and dunite were selected for detailed petrographic and microanalytical

150 geochemical investigations (Table 1). A second set of adjacent samples from the

151 clasts' centers was chosen for thin section microscopy to identify the mineralogical

152 and textural differences between clasts' rims and cores (Table 1).

153

154

155 **3. Analytical methods**

156

157 *Petrography*

158 Mineral phases were identified by polarized light microscopy. In addition, a

159 *Panalytical X'Pert PRO* X-ray diffractometer (XRD) at the University of Bremen (Cu

160 Kα radiation, 45 kV, 40 mA) was used to identify serpentine modifications in the

161 samples selected for oxygen isotope analysis (see below). Data were collected in the

162 continuous mode, between 3 to 85 °2θ, in steps of 0.017 °2θ. Spectra were

163 processed with *High-Score Plus* software.

164

165 *Electron microprobe*

166 Major element analyses of mineral compositions were performed with a *JEOL JXA-*

167 *8900* electron microprobe at the University of Kiel (Germany). For most silicate

168 minerals an accelerating voltage of 15 kV was used, with exception of garnet, spinel

169 and iron oxides (20 kV). Measurement spot sizes were typically 1-5 µm in diameter.

170 Standards were either natural minerals or synthetic materials. The CITZAF method of

171 Armstrong (1995) was used for correction of the raw counts. Micro-scale element

172 mappings and backscattered electron (BSE) images of rock microfabrics were used

173 to complement microscopic observations.

174

175 *Laser ablation ICP-MS*

176 Analyses of major and trace element concentrations were carried out on thin sections

177 by laser ablation inductively coupled plasma mass spectrometry (LA-ICP-MS) using

178 a Thermo Element2 coupled to a NewWave UP193ss (wavelength 193 nm) at the

179 Department of Geosciences of Bremen University. Helium (0.8 l/min) was used as

180 carrier gas and argon (0.8-0.9 l/min) was added as make-up gas; plasma power was

181 1200 W. Samples and standards were ablated with an irradiance of ~1 GW/cm^2, and

182 a pulse rate of 5 Hz. The laserbeam diameter was typically between 25 and 100 µm.

183 Prior to ablation the blank intensities were acquired during 25 s. All isotopes were

184 analyzed at low resolution with five samples in a 20% mass window and a total dwell

185 time of 25 ms per isotope. Depending on the mineral composition, either silicon or

186 magnesium was used as an internal standard element, which had previously been

187 determined by electron microprobe analysis. Calibration was done using glass

188 standards NIST610 and NIST612, with preferred averages from Jochum et al.

189 (2011). Analytical quality was controlled by repeated analyses of the international

190 glass standard BCR2-G (Jochum et al., 2006).

191

192 *Micro-Raman invstigations*

193   Serpentine phases were identified using a Horiba LabRAM HR confocal Raman

194   spectrometer equipped with a 532 nm laser, an astigmatic flat field spectrograph with

195   a focal length of 800 mm, and a multichannel air-cooled (-70 °C) CCD detector.

196   Spectra were collected using a 100x objective with a numerical aperture of 0.9. Two

197   diffraction gratings with 600 and 1800 grooves / mm were used. A confocal hole

198   diameter of 100 μm was chosen for most analyses. Spectra were collected for 5

199   seconds with 3-5 accumulations between 100 cm^{-1} and 1280 cm^{-1}.

200

201   *Oxygen isotope analysis*

202   For oxygen isotope analysis, serpentine minerals of the different generations were

203   separated by crushing and hand picking, and purity and mineralogy were checked by

204   X-ray diffraction (see above) and visual inspection. The oxygen isotope analyses

205   were carried out at the University of Michigan following the procedure of Alt et al.

206   (2010). Samples were reacted with BrF_5 in externally heated nickel reaction vessels

207   (Clayton and Mayeda, 1963), and O_2 was converted to CO_2 gas by reaction with

208   heated carbon rods. Oxygen isotope ratios were measured using a Finnigan Delta-S

209   mass spectrometer. These data were normalized to a value of 9.6‰ for NBS 28

210   quartz standard (± 0.2‰, 1σ), compared to the accepted value of 9.58 ‰.

211

212

213   **4. Results**

214

215   The observations presented here are based on nine extensively serpentinized

216   harzburgite and dunite clasts sampled from different depth intervals of Hole 1200A

217   (see Table 1). In particular, the clast material selected for thin section preparation

218   and analytical investigation was collected from near-rim regions that show

219   considerable influence of late-stage alteration events.

220

221

4.1 Petrography

223

The serpentinized ultramafic clasts exhibit a variety of microfabrics that range from virtually undeformed to strongly deformed (see Figs. 2 and 3). The degree of serpentinization we observed in thin section varies between 75 % and almost 100 %, but can be highly variable on the scale of centimeters. Even within the same thin section, weakly serpentinized regions can be observed adjacent to regions with abundant veins of different generations.

230

Relicts of primary olivine with average grain diameters of around 50 μm (some grains are up to 250 μm in diameter) show microgranulation and kink-banding in some areas. The size of the original olivine grains in the precursor rock was up to 3 mm. Relicts of orthopyroxene show signs of crystal deformation (undulary extinction and cleavage planes); former grains were up to 4 mm in size. Clinopyroxene is preserved as solitary crystals (diameter up to 100 μm) either in proximity to orthopyroxene, or intimately intergrown with chromian spinel. In addition, clinopyroxene is present as exsolution lamellae in orthopyroxene. In a dunite sample, spinel exhibits rhomb-shaped euhedral faces, whereas in the harzburgites studied it commonly shows embayments indicative of resorption.

241

Fabric relations

243

Serpentinization of the primary minerals led to pseudomorphic mesh and hourglass textures after olivine and bastite after orthopyroxene (and locally of clinopyroxene). Serpentine is present in veins of several generations. Besides serpentine group minerals, brucite is a common secondary phase. It is observed in intimate

248   intergrowth with serpentine in veins, and as single crystals in the centers of

249   recrystallized mesh textures.

250

251   Heazlewoodite and awaruite (Ni_3Fe) are present in trace amounts. The atomic

252   metal/sulfur ratio of heazlewoodite is near stoichiometric and varies between 1.59

253   and 1.68. Small amounts of Fe account for a representative composition of

254    $(Ni_{2.97}Fe_{0.03})S_2$. Heazlewoodite can be present in the centers of hour glass structures,

255   or as rare occurrence in veins, rimmed by awaruite. Moreover, awaruite is observed

256   on trails in the center of serpentine veins in mesh-textured olivine (Figs. 3A and B).

257   Awaruite and in a few instances wairauite (CoFe) are present in halos around type (i)

258   veins and in type (ii) veins (vein types as detailed below). Magnetite is developed in

259   early veins, which predate pervasive serpentinization as characteristic (double)

260   central vein filling (D'Antonio and Kristensen, 2004; Klein et al., 2009). Furthermore,

261   magnetite was found in late, extension-related veins as syntactically grown crystals.

262   Garnet of andraditic composition (with neglectable Al and Mg contents, and with a

263   hydroandradite (hydrogarnet) component, calculated from Si deficiency) is present in

264   two samples. It is either homogeneously distributed as small euhedral crystals (up to

265   50 μm in diameter) or clustered in anhedral crystals (individual crystals up to c. 70

266   μm, clusters up to 300 μm). In either case, garnet growth was located in mesh-

267   textured domains, commonly at the boundary between mesh core and rim.

268   Apparently, those parts of the grains growing into the mesh core developed anhedral

269   morphology, contrasting with the euhedral habit of the faces that grew towards the

270   mesh rim. A representative garnet composition is $(Ca_{2.98}Mg_{0.04})(Fe_{1.98}Al_{0.01}Cr_{0.00})$

271    $(Si_{2.81}H4_{0.19})O_{12}$, the hydroandradite component shows values between 0.14 and

272   0.27.

273

274

275   *Pervasive serpentinization*

276 Pervasive serpentinization of olivine resulted in the formation of mesh (with fresh

277 olivine in the cores) or hourglass textures (see Figs 2, and 3A and B). Former olivine

278 grain boundaries in mesh textures are outlined by awaruite; in most samples the

279 mesh texture is free of magnetite. Pseudomorphic serpentinization of orthopyroxene

280 (and locally of clinopyroxene) led to the formation of bastites. Former interstitial

281 spinel is apparently unaffected by alteration and is (in places) surrounded by

282 serpentine coronae formed from breakdown of orthopyroxene and olivine (as

283 described by Seyler et al., 2001). Brucite was not observed in pervasive mesh

284 textures. However, it is present in interstices between clinopyroxene (sub)grains, in

285 regions of mesh textures that were affected by vein serpentinization, or recrystallized

286 hourglass textures (see Figs. 2A, 2G). Serpentine in mesh textures and bastites has

287 been identified as lizardite by Raman spectroscopy (for serpentine polymorphs

288 identified in the polyphase serpentinization fabrics, see Table 4), which is consistent

289 with investigations of similar textures in other serpentinites (e.g., Dilek et al., 1997;

290 Andreani et al., 2007; Boudier et al., 2010; Pabst et al., 2011; Schwartz et al., 2012).

291

292

293 *Veins*

294 The most striking fabric element present in the clasts is the abundant veining, which

295 comprises different vein generations.

296

297 In harzburgites, several stages of veining and associated serpentinization can be

298 distinguished:

299

300 Early magnetite-bearing veins (predating pervasive serpentinization)

301 Serpentine veins containing magnetite were found in one of the thin sections studied

302 (see Fig. 2A). In these transgranular veins magnetite occurs as central vein fillings or

303 as double trails along the vein rim. This fabric type has been reported in other

304　ultramafic clasts recovered from Site 1200 (e.g., D'Antonio and Kristensen, 2004), as

305　well as in serpentinized abyssal peridotites from the Mid-Atlantic Ridge (recovered

306　from Leg 209, Hole 1274A, see Klein et al., 2009). These veins are likely an early

307　feature, preceeding and maybe initiating the pervasive serpentinization of pristine

308　ultramafic rock (Salisbury et al., 2002).

309

310　Type (i) veins

311　This vein type postdates pervasive serpentinization and features lizardite with brucite

312　and awaruite; veins are straight without marked conformance with the rock fabric

313　(see Fig. 2D1, and 2E). The walls of type (i) veins may show finger-like

314　serpentinization fronts. These "fingers" seem to emanate into interstices of mesh

315　textured domains formed during a preceeding pervasive serpentinization event. In

316　places, these veins developed mm- to cm-wide halos. In places, veins of type (i)

317　have been reactivated by later fluid fluxing events of type (iv) veins.

318

319　Type (ii) veins

320　These chrysotile-brucite veins (Table 4) encompass regions of weakly serpentinized,

321　microgranular olivine and large orthopyroxene crystals (Fig. 2B-E). They are

322　brownish in color and up to 2 mm wide. Type (ii) veins do not show a preferred

323　orientation and appear to have formed to accomodate expansion which is not related

324　to expansion during pervasive serpentinization. However, the orientation of the fibers

325　with respect to the vein walls documents an anisotropic stress field. It is unclear,

326　whether this feature represents growth or recrystallization of the vein serpentine.

327

328　Type (iii) veins

329　Extensional chrysotile veins (known as "Frankenstein" type, see e.g., Salisbury et al.,

330　2002) have developed in halos along type (i) veins (where they may intersect type (ii)

331　veins; Fig. 2D, 2E, and Table 4). They are related to the accomodation of local

332 stresses during the overall isotropic expansion of the surrounding rock. A similar vein

333 geometry has been described in detail from serpentinized orthopyroxenite dykes in a

334 dunite matrix from the Leka Ophiolite Complex, Norway (Iyer et al., 2008a, 2008b).

335

336 Type (iv) veins

337 Late-stage extensional chrysotile veins document multiple crack-seal events (as

338 described by Bons et al., 2012) either in undeformed regions with preserved granular

339 fabric, or in serpentinites hosting type (i) and (ii) veins where they crosscut and offset

340 the earlier vein generations (see Fig. 2F).

341

342 Extensional magnetite-bearing veins

343 One thin section contains magnetite, present in deformation-related extensional

344 veins, which developed as syntaxial veins from a single crack-seal event. Large

345 crystals extend from one wall to the other (as confirmed with high-resolution X-ray

346 microtomography).

347

348 Some dunites host syntaxial serpentine veins (ribbons). The ribbons separate

349 regions, in which recrystallization of serpentine and brucite can be observed (see

350 Fig. 2G). The extension accommodated by the ribbons is clearly anisotropic.

351

352

353 *Late Browning*

354 A "browning" of the clasts' margins is developed in few samples (e.g., 3R-1, 7R-2,

355 13R-2, 16R-1), which is related to an inward-migrating alteration front (Fig. 2H). This

356 browning is independent of the intra-clast fabric relations comprised by the different

357 vein generations. Browning led to high proportions of brucite in the rock that

358 proceeded either localized along former grain or sub-grain boundaries or in a

359   pervasive manner. The latter may develop by coalescence of grain boundary scale

360   replacement.

361

362

363   4.2 Mineral chemistry

364

365   *Primary minerals*

366   Olivine in both harzburgite and dunite is Mg-rich (X_{Mg} = [Mg/(Mg+Fe)] of 0.92) (Figs.

367   4A-D, Table 2), which is typical for mantle wedge peridotite (Bonatti and Michael,

368   1989; Ishii et al., 1992). Orthopyroxene has X_{Mg} values between 0.91 and 0.92, Al_2O_3

369   contents from 1.3 to 2.5 wt.%, and contains 0.6 to 1.2 wt.% Cr_2O_3 (see Figs. 4A-D,

370   and 5A-C). X_{Mg} ratios of clinopyroxene range between 0.94 and 0.95, with 0.96 - 2.02

371   wt.% Al_2O_3, and 0.24 - 1.09 wt.% Cr_2O_3. Chromian spinel is variable in composition

372   with X_{Cr} [Cr/(Cr+Al)] values between 0.48 and 0.63, and X_{Mg} ranging from 0.51 to

373   0.59 in the pervasively serpentinized regions in harzburgites.

374   In the two most strongly serpentinized harzburgites and dunites (9R-1 and 11R-1),

375   spinel approaches ferritchromite composition (X_{Cr} = 0.69 - 0.93 and X_{Mg} = 0.22 -

376   0.43). Ferritchromite is commonly regarded as an indicator of Cr-spinel alteration

377   (e.g., Mellini et al., 2005; Merlini et al., 2009; Saumur and Hattori, 2013).

378

379   *Serpentine minerals*

380   The polyphase serpentinization history of the ultramafic clasts is apparent in distinct

381   mineral compositions of the successive serpentine generations (Figs. 4A-D and 5A-

382   C). Pure chrysotile/lizardite has a molar $(Mg+Fe^{2+})$/Si ratio of 1.5. However, since the

383   majority of serpentine mineral EMPA analyses of the early vein generations of type

384   (i) and (ii) exhibits significantly lower SiO_2 and higher MgO contents, it appears that

385   minor brucite is intergrown with serpentine on a submicroscopic scale (Table 3).

386

387   Compositions of pseudomorphic serpentine minerals formed during the pervasive

388   serpentinization phase were found to be indicative of their precursor mineral in terms

389   of Al_2O_3 and CaO contents of the serpentine phase (Fig. 5A-C). Serpentine in mesh

390   and hourglass textures has X_{Mg} values of 0.90 - 0.94. Serpentine in mesh and

391   hourglass textures does contain as little Cr_2O_3 as the olivine precursor, but exhibits

392   higher Al_2O_3 and CaO as olivine. These serpentines in harzburgites (Al_2O_3 > 0.1 to <

393   1.0 wt.%, CaO: 0.1 - 0.6 wt.%) tend to be richer in both components than dunites

394   (Al_2O_3 < 0.1 wt.%, CaO: 0.08 - 0.2 wt.%). In recrystallized hourglass textures in

395   dunite, the X_{Mg} of serpentine coexisting with brucite is slightly higher (0.94-0.96) than

396   X_{Mg} of serpentine in unrecrystallized regions. No differences between mesh rim and

397   core compositions have been observed. Bastite textures consist of serpentine, with

398   X_{Mg} values between 0.89 - 0.94. Most bastites retain the high Al_2O_3 contents (> 1.0

399   wt.%), as well as the CaO (0.1 - >1.0 wt.%) and Cr_2O_3 (0.1 - 1.0 wt.%) values of the

400   pyroxene precursor (see Fig. 5A-C). Analyses of serpentine in halo regions of type (i)

401   veins and in type (ii) veins show marked SiO_2 deficits (Fig. 4B-C), indicating

402   intergrowth with submicroscopic brucite, and low X_{Mg} values (an average X_{Mg} of 0.80

403   in Brc-Srp intergrowth, and down to X_{Mg} of 0.40 in coexistence with Cpx).

404   Serpentinites in the halos of type (i) veins show identical contents of Al_2O_3 and CaO

405   as the pseudomorphs outside the halos. Serpentine in type (iii) and type (iv) veins

406   shows SiO_2 contents expected for pure serpentine and X_{Mg} values of 0.89 - 0.96 (see

407   Fig. 4D). Later veins of type (ii)-(iv) also exhibit the characteristic Al_2O_3 and CaO

408   contents of the pseudomorphs present in their host rocks (see Fig. 5A-C).

409

410   Using Micro-Raman investigations of the polyphase serpentinization fabrics, we have

411   identified two serpentine polymorphs: Lizardite and chrysotile (see section 4.1 and

412   Table 4). Lizardite has been found in the rims of mesh textures, surrounding olivine

413   cores, and in bastites. Moreover, it is present in mesh/hourglass and bastite

414   pseudomorphs in regions that were affected during the halo formation around type (i)

415 veins. Later vein generations (type ii-iv) are comprised of chrysotile. In the clasts

416 investigated by micro-Raman, no antigorite was identified.

417

418 *Brucite*

419 Brucite is present either as readily identifiable crystals (up to 100 μm diameter) in

420 interstices or recrystallized areas, or fine-grained as vein fill. The occurrence of

421 brucite submicroscopically intergrown with serpentine minerals has been recognized

422 from microprobe analyses based on SiO_2 deficits, MgO excesses, and low totals (see

423 above, and Table. 3). Brucite-serpentine intergrowths in harzburgites were also

424 observed in type (i) and type (ii) veins and point to brucite compositions of $X_{Mg,Brc}$

425 0.79 - 0.85. Brucite is apparently lacking in the pervasive serpentinization stage as

426 well as in type (iii) and in type (iv) veins.

427

428 In harzburgites, interstitial brucite is present in type (i) veins or halos, typically with

429 MnO contents from 0.19 to 0.53 wt.%, and X_{Mg} values between 0.79 and 0.90. In

430 places, type (i) veins contain brucite with slightly elevated MnO contents between

431 0.94 and 2.20 wt.% and low X_{Mg} values of 0.59 - 0.63 (these MnO values correspond

432 with brucite analyses given in D'Antonio and Kristensen, 2004). A single occurrence

433 of brucite in contact with clinopyroxene features 1.65 to 2.19 wt.% MnO and X_{Mg}

434 values between 0.36 and 0.47. In dunites, single crystals of brucite can be observed

435 where cores of hourglass textures have recrystallized (Fig. 2G). The X_{Mg} values of

436 the recrystallized brucite range between 0.83 to 0.85.

437

438

439 4.3 Trace element mineral chemistry

440

441 Trace element concentrations of serpentine provide insights into potential precursor

442 phases and compositions of serpentinization fluids.

443

444 Ni and V contents of serpentine are different for olivine and pyroxene precursors.

445 Figure 6A shows that serpentine (or regions of serpentine-brucite intergrowth)

446 formed at the expense of olivine can contain up to 0.5 wt.% Ni (with an average

447 around 0.3 wt.%), corresponding to the Ni content of the primary olivine. Or rather, Ni

448 is most likely measured as fine-grained awaruite, present in the laser-ablation spots).

449 In contrast, bastite-serpentine (i.e. orthopyroxene precursor) has < 0.1 wt.% Ni,

450 corresponding to the average Ni concentration of ortho- and clinopyroxene (c. 700

451 ppm). Likewise, V concentrations of serpentine (Fig. 6B) replacing olivine are mostly

452 below 1 ppm, which reflects the V concentration of its precursor. In bastite textures,

453 V contents are up to 80 ppm, corresponding to 60-80 ppm V in orthopyroxene. On

454 rare occasions, bastitization of clinopyroxene has been observed in completely

455 serpentinized clast rims (identified by the shape of the former grain). Here, vanadium

456 contents are slightly higher as in orthopyroxene bastites (60-120 ppm). The Ni-V

457 variation diagram (Fig. 6C) shows the discriminatory significance of these trace

458 elements in identification of the serpentine parent mineral. The variation in the Cr-Ni

459 diagram (not shown) is identlical apart from the higher absolute concentrations of

460 chromium (section 4.2), corresponding with data from Kodolanyi et al. (2012).

461

462 B, Ba, Sr, Rb and Cs data of regions with submicroscopic intergrowth of serpentine

463 and brucite show increasing trace element concentrations with increasing

464 Si/(Mg+Fe)-ratio, which indicates that these elements are incorporated in the

465 serpentine structure and are not present in brucite (Figs. 7A-E). Therefore, the

466 element concentrations of the mixed analyses of serpentine-brucite regions have

467 been recalculated to pure serpentine (indicated by the curved lines in Figs. 7A-E).

468

469 Regardless of the nature of the precursor phase and presumed formation stage, all

470 serpentinization products are enriched in B (Figs. 7A and 7F), and calculated

471   serpentine endmember compositions have up to 200 ppm boron (mostly between 80-

472   100 ppm). Ba, Sr, Rb, and Cs are also commonly enriched in the serpentinization

473   products and veins relative to the precursor phases (Fig. 7B-E). In contrast to B,

474   however, these elements show distinct differences in concentration between

475   serpentine formed during different stages of veining and fluid-rock interaction. Most

476   notably, early vein generations show high trace element concentrations compared

477   with later veins (Table 4).

478

479   On average, serpentine of the early serpentinization stages (i.e., in mesh rims of

480   pervasive stage, in type (i) veins, or in the halo around type (i) veins) exhibit a strong

481   enrichment in Rb (0.8 ppm), Cs (0.4 ppm), Ba (> 10 ppm), and Sr (> 50 ppm). For Ba

482   and Sr the enrichment is unrelated to the nature of the precursor mineral, while

483   bastites, and interstitial serpentine of regions with only weakly serpentinized

484   orthopyroxene and microgranular olivine crystals, have even higher concentrations of

485   Rb (up to 2.6 ppm) and Cs (up to 1.2 ppm; Figs. 7D and E). In the later vein

486   generations, remarkable differences in the enrichment of either (Rb and Cs) or (Ba

487   and Sr) occur. In type (ii) veins, average Ba (3.7 ppm, up to 11.3 ppm) and Sr (13.6

488   ppm, up to 27.7 ppm) concentrations are also high. In type (iii) and (iv) veins,

489   serpentines show average concentrations of Ba (0.4 ppm) and Sr (3 ppm), which

490   markedly lower than in the earlier vein generations (types i and ii), but still

491   significantly higher than those of the primary minerals (Figs. 7B and C). In contrast,

492   the average concentrations of Rb and Cs in serpentines of type (ii)-(iv) veins are low

493   (<0.1-0.3 ppm) and similar to those of the primary phases Figs. 7D and E).

494

495

496   4.4 Oxygen isotope compositions of serpentine minerals

497

498 The measured oxygen isotope compositions of serpentine minerals range between

499 6.1 and 10.5 $\delta^{18}O$, consistent with serpentinite clasts from Conical, Torishima, and

500 Ogasawara Seamounts (Alt and Shanks, 2006; Sakai et al., 1990). Table 5 provides

501 an overview of the oxygen isotope data for the mineral separates along with details

502 about mineralogical composition of the different samples (as determined by XRD

503 analyses). The oxygen isotope data do not show significant differences between

504 different vein generations or serpentine polymorphs. Note that two mineral separates

505 contained a noticeable fraction of brucite (16R-2).

506

507

508 **5. Discussion**

509

510 *5. 1 Low-temperature serpentinization conditions in the Mariana mantle wedge*

511

512 The serpentinized ultramafic clasts exhibit a variety of microfabrics that indicate a

513 polyphase serpentinization history. A common feature during all stages of

514 serpentinzation is that little magnetite was formed (if at all). In contrast to samples

515 from mid-ocean ridge settings, mesh textures lack magnetite tracing former olivine

516 (sub-)grain boundaries. Instead, the serpentinized ultramafic clasts are composed of

517 serpentine ± brucite ± iron alloys (mostly awaruite). This magnetite-free assemblage

518 has been found as late-stage formation in rocks from magma-poor rifted continental

519 margins (Beard et al., 2009), in the forearc of subduction zones (Lafay et al., 2012),

520 and in low-temperature serpentinization experiments (batch reactor: Seyfried et al.,

521 2007; flow-through experiment: Godard et al., 2013). In a recent study, Klein et al.

522 (2014) propose that decreasing abundance of magnetite is indicative of decreasing

523 alteration temperatures. Instead of magnetite, Fe-rich brucite forms at temperatures

524 below ca. 200℃ (cf. Klein et al., 2009). These low formation temperatures would be

525 consistent with temperatures predicted for a depth of 25 km by models of the thermal

526 structure of a cold oceanic subduction zone (Izu-Bonin, see Hyndman and Peacock,

527 2003).

528

529 Metabasite clasts may serve as an additional constraint on p,T-conditions that prevail

530 at the slab-mantle interface recorded at variable depth levels reaching from

531 intermediate to near the base of the conduit of the mud diapir. In the case of South

532 Chamorro Seamount and Conical Seamount, metabasite schists indicate low

533 temperatures of 250-300 ℃ (at a pressure of •0.4-0.50 GPa; Fryer et al., 2006) and

534 ~175-250 ℃ (at a pressure of 0.5-0.65 GPa; Maekawa et al., 1993), in depths

535 slightly above the base of the feeding conduits.

536

537 The $\delta18O$ values for serpentine in this study (6.1 to 10.8 ‰) are similar to those from

538 Conical seamount and to those dredged from Torishima and Ogasawars Seamounts

539 (Sakai et al., 1990; Alt and Shanks, 2006). Using oxygen isotope fractionation

540 between serpentine and magnetite, Alt and Shanks (2006) calculated higher

541 temperatures of 300-375 ˚C for serpentinite clasts from Conical Seamount. The

542 dominance of antigorite in some of the Conical Seamount samples suggests that

543 higher estimated temperatures may be real, as antigorite is stable at higher

544 temperatures (above 300 ˚C, Schwartz et al., 2012), but these temperature estimates

545 were based on mineral separates from bulk rocks (Alt and Shanks, 2006), which

546 integrate multiple stages of serpentinization and magnetite formation, leading to

547 larger uncertainties. In the rocks studied in this work, no pairs of coexisting

548 serpentine and magnetite were at hand for temperature estimation. Since the

549 presence of magnetite is restricted to scarce occurrence in vein types not related to

550 the main serpentinization phases (see above), it is not very likely, that a magnetite

551 separated from bulk rock powders would be coeval with chrysotile separated from

552 late veins. Rather, fluid-rock ratios, the fluids as such, and maybe also the

553 temperatures prevalent at early mesh formation (yielding magnetite, given

554 appropriate conditions) would differ from late-stage conditions governing the

555 formation of late-stage, extensional chrysotile veins. However, by constraining some

556 boundary conditions for the fluid-rock interaction we can estimate serpentinization

557 temperatures of the 1200A clasts.

558

559 Using the serpentine-water oxygen isotope fractionation from Saccocia et al. (2009),

560 temperatures of 175-240 °C are calculated assuming equilibrium between serpentine

561 in Table 5 and fluids sampled from South Chamorro seamount ($\delta^{18}O$ = +2.5‰; Fryer

562 et al., 2006). Lower temperatures of 145-200 °C are calculated assuming equilibrium

563 with seawater (0‰). Stable isotope compositions of serpentinites from Conical

564 seamount indicate derivation of serpentinizing fluids from the subducting slab (Alt

565 and Shanks, 2006). If serpentinizing fluids contained a component of sediment pore

566 waters, which have negative $\delta^{18}O$ values (Lawrence and Drever, 1981), then

567 equilibrium temperatures for serpentine are even lower (125-170 °C for -2‰ fluid;

568 Saccocia et al., 2009). These temperature estimates are consistent with low

569 temperatures inferred from mineralogy of Chamorro samples and with thermal

570 models for cold subduction (Klein et al., 2009; Hyndman and Peacock, 2003).

571

572 The above estimates suggest relatively low temperatures (below 250 °C) for the

573 serpentinite samples from South Chamorro seamount (Site 1200, distance from

574 trench: 85 km), which seemingly is in contrast to the higher serpentinization

575 temperatures of 300 - 375 °C estimated for samples from Conical seamount (Site

576 780, distance from trench: 90 km; distance from Site 1200: almost 1000 km) by Alt

577 and Shanks (2006). While the high-temperature polymorph antigorite is the dominant

578 serpentine phase in several samples from Conical seamount, it is scarce in South

579 Chamorro and other Mariana forearc seamounts (see section 5.2). On the contrary,

580 the absolute concentrations of Cs, Rb, Ba, and Sr observed in serpentine in this

581   study indicate that the serpentinizing fluids of the South Chamorro samples derive

582   from sediment dehydration at temperatures of $\sim$ 150 ℃ (section 5.3), similar to the

583   estimations by Alt and Shanks (2006) for Conical. We consider this an expression of

584   both a differing subduction zone geometry and the variation in the thermal structure

585   of the slab and wegde: the mud volcanoes can sample the entire thickness of the

586   wedge, and can include samples from any time within the 40 million year history of

587   the subduction zone. So they could include early higher-temperature serpentinites,

588   which could be one explanation for high-temperature samples at Conical seamount.

589   Certainly in a "mature" subduction zone, without mantle counterflow in the wedge,

590   the low temperatures as shown by the Chamorro samples are expected. Moreover,

591   the source region of the ultramafic material mobilized as clasts and erupted in mud

592   flows does not necessarily lie within the wedge. Besides serpentinization of conduit

593   wall rock, also material from the basal plane of the suprasubduction mantle wedge,

594   partly serpentinized and eroded in shallower parts of the decollement, may rise

595   through the conduit system and be erupted within the mudflows (section 5.4).

596

597

598   *5.2 Textures and serpentine polymorphs*

599

600   Different low-temperature serpentine polymorphs are common in serpentinized

601   abyssal peridotites. In the present work, micro-Raman investigations demonstrate

602   the occurrence of two serpentine polymorphs in distinct textural context. Lizardite is

603   present in the rims of mesh textures, surrounding olivine cores, in bastites, and in

604   early type (i) veins. Later vein generations are comprised of chrysotile. Antigorite,

605   which is commonly seen as indicative for higher-temperature serpentinization, could

606   not be identified. In previous studies of ultramafic clasts from ODP Leg 195, Site

607   1200 (D'Antonio and Kristensen, 2004; Pabst et al., 2011), lizardite and chrysotile,

608   but not antigorite, were identified. At Conical Seamount, Ishii et al. (1992), and

609   Saboda et al. (1992) observed antigorite in thin sections of serpentinized dunite

610   (Hole 780C) and harzburgite clasts (Hole 779A). Alt and Shanks (2006) observed

611   antigorite in serpentinized harzburgites and dunites from Site 779 and 780, being the

612   dominant serpentine phase in several samples. In contrast, antigorite was putatively

613   identified by Fryer and Mottl (1996) in muds at Holes 778A and 779 A (in 3 out of 16

614   samples) but appears absent in Site 780 muds. As stated in Savov et al., (2005a),

615   scarcity or absence of antigorite in the Mariana forearc serpentinites (apart from

616   Conical Seamount) are noted by many authors (e.g., Saboda et al., 1992; Zack et al.,

617   2004; Murata et al., 2009; Pabst et al., 2011), while chrysotile and lizardite are

618   common.

619

620   In numerous studies of oceanic serpentinites, the growth of distinct serpentine

621   polymorphs under different reaction conditions (e.g., varying water rock ratios,

622   tectonic regimes etc.) was noted. For instance, lizardite in rims around olivine mesh

623   centers, and in bastites, has been reported from the mid-ocean ridge Site 920, e.g.,

624   by Dilek et al., (1997, by XRD), Andreani et al., (2007, by TEM; 2013, by Raman),

625   from Sites 1272 and 1274 by Kodolanyi et al., (2012, by Raman), and from

626   ophiolites, e.g., by Boudier et al., (2010, TEM), Hirauchi et al., (2010, Raman), and

627   Schwartz et al., (2012, Raman). The clasts from Mariana forearc mantle may exhibit

628   a great diversity with respect to (i) the differing degree of serpentinization, (ii) the

629   differences in the source regions within the mantle wedge, and (iii) the relative timing

630   of serpentinization stages in the individual clasts. Pabst (2009) found either lizardite

631   or chrysotile both in mesh rims and mesh centers, and also the occurrence of

632   polygonal serpentine is reported. Pabst (2009) found bastites composed of lizardite,

633   in other samples of polygonal serpentine. Kodolanyi et al. (2012) reported the

634   occurrence of lizardite in mesh rims and bastites, and of chrysotile in mesh centers

635   and bastites. In the present study, lizardite has been found in early serpentinization

636   textures, and chrysotile in intermediate and late vein generations.

637

638   In most of the aforementioned studies, chrysotile has been found in extensional

639   veins, crosscutting pervasive serpentinization and in earlier vein generations.

640   Furthermore, Andreani et al., (2007, 2013), mention the involvement of polygonal

641   serpentine in the vein mineralization. In general, the preferential occurrence of

642   chrysotile in expansional regimes with higher water-rock ratios has also been noted

643   for the ultramafic clasts from the Mariana forearc mud volcanoes (e.g., D'Antonio and

644   Kristensen, 2004; Pabst et al., 2011; and described in more detailed by Pabst, 2009).

645

646   In the present study, the pseudomorphic serpentinization textures suggest that early

647   pervasive serpentinization took place under static conditions (e.g., Wicks and

648   Whittaker, 1977; O'Hanley 1996), yielding isotropic expansion. In the course of the

649   successional veining events, the expansional regime gradually became more

650   anisotropic. The formation of type (i) veins points to clearly anisotropic stress,

651   however related to merely minor expansion. Type (ii) veins do not show a preferred

652   orientation and appear to have accomodated considerable overall isotropic

653   expansion. The extensional chrysotile veins of the "Frankenstein" type (iii) veins

654   accomodate local stresses in the halos along type (i) veins, associated with the

655   overall isotropic expansion of the surrounding rock. Late-stage extensional type (iv)

656   chrysotile veins formed in a clearly anisotropic stress regime and led to anisotropic

657   expansion, documented as multiple crack-seal events (as described by Bons et al.,

658   2012).

659

660

661   *5.3 In-situ mineral analyses reveal distinct FME patterns for successive*

662   *serpentinization events and potential fluid source rocks*

663

664   Since the proportions of the different serpentine generations in the bulk sample and

665   the fraction of brucite in Srp-Brc intergrowth regions are highly variable, it is difficult

666   to unravel the formation history of the clasts using trace element contents of bulk

667   rocks. For instance, Savov et al., (2007) observed no correlation between the degree

668   of serpentinization (expressed as LOI wt.%) and the abundance of FME and Th. The

669   detailed mineral analyses of serpentine, in contrast, facilitate the recognition of

670   different trace element contents in distinct veins and microfabrics, which can be

671   linked to distinct episodes in the polyphase serpentinization history of mantle

672   material.

673

674   The observed trace element contents in the clasts from South Chamorro Seamount

675   decrease with progressive serpentinization. These elements are incorporated in the

676   serpentine structure and are not present in brucite (Figs. 7A-E; section 4.3). While

677   later serpentinization stages recorded in the clasts - and the trace element

678   concentration measured in serpentine of the mud matrix - are characterized by

679   decreased FME concentrations, both bastites and interstitial serpentine in

680   microgranular olivine regions formed during preceding serpentinization events share

681   higher FME contents.

682

683   In order to explain the observed variation of serpentine trace element concentrations,

684   selected mineral analyses are compared with literature data on related bulk rock and

685   fluid compositions (Fig. 8). Concentrations of Cs and Rb (Fig. 8A) from the late

686   serpentine type (iii) and type (iv) are similar to the Cs/Rb values reported by Savov et

687   al. (2007, and 2005) for the mud matrix. In contrast, products of all earlier veining

688   and serpentinization events yield higher Cs and Rb values, which are similar to the

689   variation of bulk compositions reported by Savov and coworkers for the serpentinized

690   clasts. The same systematic difference can be seen in the concentrations of Sr and

691   Ba (Fig. 8B). Trace element contents of sediments (from Plank and Langmuir, 1998)

692   and variously altered oceanic crust (AOC; Kelley et al., 2006) as potential source

693   rocks of the serpentinizing fluids are also plotted in Fig. 8, together with analyses of

694   "fresh peridotite" from Meffré et al., (2012).

695

696   Rb, Cs, Sr, and Ba concentrations in sediments are higher than in both mud matrix

697   and serpentine veins in the clasts. Altered oceanic crust (AOC) may have higher Sr

698   and Ba contents than either mud matrix or clast serpentine, and may show similar Cs

699   contents as the mud matrix and serpentine in clasts, depending on the alteration

700   stage. However, AOC contains slightly less Cs than the early clast serpentine

701   generations. In contrast, Rb concentrations of strongly altered oceanic crust may be

702   higher than those of mud and late clast serpentine, and even higher than those of

703   early clast serpentine generations. Thus, both sediments and altered ocean crust

704   could serve as source for higher Sr and Ba values in the serpentinizing fluid, but only

705   sediments and very highly altered oceanic crust can be considered to discharge high

706   Cs,Rb fluids. The main sources of fluid to be released in a low-T environment such

707   as the forearc region of a cold subduction zone are thought to be related to sediment

708   compaction and from sediment dehydration reactions involving opal (at 30 - 80 °C)

709   and smectite (120 - 150 °C; see Hyndman and Peacock , 2003; Fryer and Salisbury,

710   2006), with little or no participation of AOC as fluid source.

711

712   The mobilization of volatiles (B and NH_4) and incompatible elements (As, Be, Cs, Li,

713   Pb, Rb) in hydrothermal fluids at relatively low temperatures ($\sim$ 300 °C) was

714   demonstrated by You et al. (1996) in laboratory hydrothermal autoclave experiments

715   with sediments of the decollement zone at Site 808 in Nankai Trough, Japan. The

716   absolute concentrations of Cs, Rb, Ba, and Sr observed in serpentine in this study,

717   indicate that fluids derived from sediment dehydration may account for high trace

718   element contents in serpentine formed during the pervasive stage and the early vein

719   generations. Regardless of the absolute Cs and Rb contents of lizardite and

720 chrysotile, the observed Rb/Cs ratios are fairly uniform within the different serpentine

721 generations and average between 1 and 10 (average Rb/Cs ratios in early

722 serpentines (mesh, bastites, vein types I and II) are between 2-4, associated with

723 high absolute elemental concentrations; late serpentine exhibits averaged Rb/Cs

724 ratios of 7 (type III) and 8 (type IV), associated with low absolute elemental

725 concentrations; Fig. 8A). It is possible that subducted sediments containing a high

726 fraction of pelagic clays release fluids high in Rb and Cs, and account for the high

727 trace element contents of serpentine formed in the pervasive stage and the early

728 vein generations. The uniformly low Rb/Cs ratios $\leqq$10 observed in the serpentine

729 minerals from Site 1200A are consistent with a sedimentary origin of the

730 serpentinizing fluids, which were released at low to moderate temperatures (50 - 300

731 $°C$), indicating a higher mobility of Cs relative to Rb.

732

733 The systematic variation of trace element contents of pore fluid compositions of

734 several seamounts with distance from the Mariana trench, revealed in geochemical

735 studies (Fryer et al., 1999; Mottl et al., 2003, 2004; Hulme et al., 2010), support the

736 hypothesis of sediments as a main source of slab fluids in the forearc region. Figures

737 8A and 8B shows the trace element contents of the pore fluids from South Chamorro

738 and other Mariana forearc seamounts as summarized in Mottl et al. (2004). Water

739 compositions from the following seamounts, in the order of increasing distance from

740 the trench, are also plotted: Bottom seawater (distance: 0 km), Pacman Baseball Mitt

741 (52 km), Blue Moon (55 km), Pacman summit (64 km), Big Blue (70 km), S.

742 Chamorro S351 spring (85 km), Seamount Site 1200 (85 km), and Conical Site 780

743 (90 km). The observed concentrations are consistent with increased mobilization of

744 trace elements from sediments with increasing temperature and depth of slab, as

745 predicted for cold subduction zones (Hyndman and Peacock, 2003; Plank and

746 Langmuir, 1998; Fryer, 2012, and references therein). The accuracy of these

747 predictions is also supported by the similarity of the fluids in terms of Rb and Cs (Fig.

748 8A) observed in the experimental charges of You et al. (1996). The Ba concentration

749 might be influenced by complex interactions with sulphate (Fig. 8B). Admittedly,

750 although the fluids discharged in experimental runs document the mobilization of

751 trace elements from solids into the fluid phase, the fractionation of trace elements

752 into the secondary minerals during serpentinization is unknown. However, as

753 indicated by the similarity in trace element contents of late-stage vein and mud

754 serpentine, the fluids constituting the mud might be quite similar to those of the late

755 stages of serpentinization. A caveat of this interpretation is that the different fluid

756 advection velocities in the different seamounts and different extents of seawater

757 entrainment and mixing/precipitation (ie. of aragonite, affecting Sr concentrations)

758 cannot be considered.

759

760 South Chamorro's pore water samples document the accumulated trace elements in

761 the fluid present in the subduction channel beneath the mud volcano, mobilized at all

762 temperatures and depths prevailing between trench and conduit. The multiphase

763 serpentinization events observed in the erupted clasts possibly also document the

764 release of serpentinizing fluids at different levels of the decollement: both microfabric

765 observations on the clasts and trace element analyses of the solids erupted by the

766 forearc mud volcanoes indicate a change in the fluid regime. On the one hand,

767 serpentines of the pervasive serpentinization stage and early vein generations

768 formed under low water/rock ratios and are characterized by high trace element

769 contents and Rb/Cs between 1 and 4. In contrast, serpentines in late extensional

770 veins and in the mud formed under higher water/rock ratios, and exhibit still high, but

771 slightly reduced trace element contents with a slightly increased Rb/Cs ratio near 10.

772 Thus, the increasing Rb/Cs ratio observed in successive serpentinization events

773 track the transformation of the compositional pattern of the slab-sourced fluids, being

774 progressively released and accumulated during continued subduction (e.g., Bebout

775   et al., 2007). In this context, late vein serpentine and mud would represent

776   serpentinization in greater depth nearer to the conduit, while serpentinization of the

777   pervasive stage and the early vein generations might have taken place in shallower

778   parts nearer to the trench. This is consistent with several studies of the Mariana

779   mudflow systems, that have mentioned the possibility that serpentinites formed at

780   shallower levels of the decollement might been carried in deeper parts of the

781   subduction zone, where they would contribute to magma genesis at the arc and

782   backarc regions (Kerrick and Connoly 2001; Savov et al., 2005b, 2007; Snyder et al.,

783   2005; Wei et al., 2005). Thus, clasts and matrix erupted at the mud volcanoes

784   represent a snapshot of these process.

785

786

787   *5.4 Generic model for the polyphase serpentinization history of Mariana forearc*

788   *mantle clasts*

789

790   The mantle wedge of a cold oceanic subduction zone imposes distinct boundary

791   conditions for fluid migration and mineral-fluid interaction at shallow levels. While the

792   fresh and cold mantle of the tapering wedge would not likely allow mantle convection,

793   the rheology of the serpentinized ultramafic rocks may confine the passage of fluids

794   to fracture bound focused flow, localized around faults or conduits (Fryer, 2012)

795   feeding the serpentine mud volcanoes. Concerning the interaction between mantle

796   and subducting plate, the location of the decoupling-coupling transition (Furukawa,

797   1993) is of fundamental importance for the advance of serpentinizing reactions in the

798   Mariana forearc mantle. Hyndman and Peacock (2003) propose a thermal structure

799   of a cold oceanic subduction zone (Izu-Bonin), with temperatures in the supra-

800   subduction mantle well below 300 $°C$. These authors suggest that a decreased

801   coupling between the subducting plate and mantle wedge is due to serpentinization

802   at the base of the mantle wedge seaward of the arc. Hyndman and Peacock (2003)

803 furthermore propose that the weak rheology and positive buoyancy of serpentinite

804 will act to isolate hydrated forearc mantle from the overall mantle wedge flow system.

805 By focusing shear deformation in the weak, serpentinized mantle adjacent to the

806 subducting plate, suprasubduction mantle and downgoing slab are mechanically

807 decoupled at the plate interface. This idea is corroborated by findings of simple-shear

808 experiments at a temperature of 200 °C and a pressure of 1.0 GPa (Hirauchi et al.,

809 2010), indicating that the dominant flow mechanism of mesh-textured serpentine

810 (lizardite and chrysotile) evolves with increasing shear strain from inhomogeneous

811 semi-brittle flow to homogeneous ductile flow, rather than faulting, brecciation, or

812 fracturing. Moreover, the confirmation of plastic flow by intracrystalline deformation

813 within individual serpentine grains by Hirauchi et al. (2010) is consistent with textural

814 features observed in highly deformed natural serpentinites (i.e., ribbon texture; Viti

815 and Mellini, 1998; Hirauchi and Yamaguchi, 2007). More recently, deformation

816 experiments on lizardite (in the range of 150-400 °C, 1-8 GPa at varying strain rates)

817 and combined first-principles calculations of Amiguet et al. (2012) revealed strain-

818 rate independent plasticity of lizardite at low stress. Even at the potentially high strain

819 rates prevalent at the shallow mantle wedge (10-20 km depth) of a cold intra-oceanic

820 subduction zone, lizardite is capable of a strain localization into cm-scale shear

821 bands, which provides a plausible mechanism for mobilization of rock fragments in

822 shallower parts of the decollement (Hirauchi et al., 2010).

823

824 Two source regions of ultramafic material, mobilized as clasts and erupted in mud

825 flows, seem possible: (i) serpentinization of conduit wall rock and mobilization as

826 clasts in the mud flow, and (ii) clasts of material from the basal plane of the

827 suprasubduction mantle wedge, partly serpentinized and eroded in shallower parts of

828 the decollement. In scenario (i), fluids serpentinizing the conduit wall rocks would

829 derive from the rising mud. The FME-enrichments characteristic of the early phase of

830 serpentinization would imply a temporal change of the FME-contents of these mud

831 fluids that passing up the conduit, because none of the later generations of
832 serpentinite show this enrichment. Such an oscillation of the degree of FME-
833 enrichment in the mud rising through the conduit systems must have produced
834 likewise clasts with an FME-enrichment pattern reversed to what is actually
835 observed: low-FME concentrations in an early pervasive phase, and high-FME
836 concentrations in late vein stages, and large amounts of high-FME mud serpentine.

837

838 However, bulk analyses from clast and mud material (Savov et al., 2005a and 2007)
839 and the analyses of individual serpentine generations in this work uniformly show
840 higher FME in the clast serpentines than in the mud. It is not likely that the mantle
841 rocks forming the conduit walls beneath South Chamorro Seamount first were
842 serpentinized pervasively by fluids emanating from the slab-mantle interface with
843 high-FME concentrations, which then shift to lower FME-concentrations in the later
844 stage of mobilization and massive mud rise. This shift in the trace element signature
845 of the serpentinizing fluid is more plausibly explained by the second scenario outlined
846 above. Mantle material of the basal plane of the suprasubduction mantle wedge is
847 partly serpentinized by fluids derived from the slab sediments in shallower parts of
848 the decollement. These fluids have uniformly high-FME contents which is inherited
849 by the rocks altered during these early serpentinization stages. During descent to the
850 depth of the conduit beneath South Chamorro Seamount, the continued release of
851 fluids from the slab might alter the level of FME-enrichment of the fluid present in the
852 subduction channel that likewise govern the serpentinization of the later clast vein
853 generations and the mud matrix serpentine.

854

855

856 *5.5 Summarized microfabric evolution of the polyphase serpentinization of Mariana*
857 *forearc mantle clasts*

858

859   Figure 9 presents a schematic view of the relative chronology of the microfabric

860   evolution, summarizing the observed fabric relations of the polyphase

861   serpentinization history of Mariana forearc mantle. The first serpentinization event is

862   believed to have occurred along a discrete set of tiny fractures (mostly < 10 mm)

863   activated by regional brittle deformation (Salisbury et al., 2002), along which

864   formation of magnetite trails can be observed (see Fig. 9A, early magnetite veins).

865   This event was followed by a stage of pervasive serpentinization with low water-rock

866   ratios, which proceeded under a static, isotropic pressure regime, which led to the

867   development of mesh structures and bastitization of orthopyroxene (Fig. 9B). The

868   serpentine formed during this stage (lizardite) has likely been exposed to a relatively

869   unaltered sediment-derived fluid derived from the sedimentary covering the

870   subducting slab, which contained high concentrations of Cs, Rb, Sr and Ba.

871

872   The pervasive phase was followed by a phase of the establishment of fluid pathways,

873   generating focused fluid flow along reactivated early magnetite veins, or newly

874   developed type (i) veins, involving occasional isovolumetric metasomatism (SiO_2-loss

875   and halo formation; see Fig. 9C). Metasomatism did not alter the trace element

876   contents present in the serpentine component in Srp-Brc regions. Later

877   serpentinization events document the loss of confining rock pressure and the onset

878   of volumetric expansion (see Fig. 9D) and the shift to higher water-rock ratios,

879   preluding the change from a rock-dominated to a fluid-dominated system:

880   extensional chrysotile veins of type (ii) contain a significant Brc fraction (see Fig. 4C)

881   with intermediate to low Cs and Rb contents, and high Ba and Sr content which are

882   comparable to serpentine of earlier phases. Most probably, the mobilization of wall

883   rock fragments into the mudflow (either in subduction channel or within conduit)

884   involves a transition from a closed system to an open system by development of fluid

885   pathways, similar to the sequence of serpentinization during unroofing of mantle in

886   slow-spreading mid-ocean ridge environments (Andreani et al., 2007).

887

888   Further expansion of the rock in the course of continued serpentinization could not

889   be followed by the already completely serpentinized halo at the rim, and this lead to

890   the formation of type (iii) "Frankenstein" veins (see Fig. 9E; Salisbury et al., 2002;

891   see also Iyer et al., 2008b). The serpentine (chrysotile) formed in this phase, and the

892   multiple crack-seal chrysotile veins of type (iv), which document marked anisotropic

893   expansion (see Fig. 9F), exhibit low trace Cs, Rb, Ba, and Sr contents which are

894   comparable to those of bulk mud analyses of Savov et al., (2005), and to spring or

895   pore water compositions of Site 1200. The type (iv) veins we could observe in our

896   samples are located in the rim regions of clast samples 3R-1_3-7, 16R-1_52-54, and

897   16R-2_7-9. The serpentine formed in both of the later vein generations documents a

898   further change in the serpentinizing fluids, suggesting a diminished influence of

899   solely sediment-derived fluids.

900

901   Microfabric information, phase relations (occurrence of the serpentine polymorphs

902   lizardite and chrysotile; presence or absence of brucite) and the correlation of FME-

903   concentrations of the successive serpentinization stages of the Mariana forearc

904   mantle clasts imply some constraints on the nature of the serpentinizing fluids. The

905   absence of brucite in the early serpentinization phase may be explained by the

906   quartz-saturated nature of unaltered sediment-derived fluids. Opal and smectite

907   dehydration produce high-FME (with $Rb/Cs < 10$; You et al., 1996), quartz-saturated

908   fluids that may initiate early pervasive serpentinization processes at shallow levels.

909   During the continued serpentinization in a still rock-dominated environment, brucite

910   becomes more common, because the high-FME-fluids are either consumed or

911   depleted by early pervasive serpentinization. Eventually, late chrysotile veins (types

912   iii and iv, in which brucite is absent) document the increased access of slab fluids in

913   a now fluid-dominated serpentinization regime. These fluids are still quartz saturated,

914   but geochemical slab signatures in trace elements are lacking, because the

composition of slab-derived fluids has been completely reset by serpentinization reactions and continued diagenetic to metamorphic processes within the subduction channel (Moore and Saffer, 2001). The final stage of diapiric rise of matrix and clasts in the conduits feeding the mud volcanoes is characterized by a very late alteration feature (see Fig. 2H, or also Fig. F78 in Salisbury et al., 2002). Apparently, the "browning" of the clasts from the rim inward (independent of the intra-clast fabric relations) corresponds to re-equilibration with the rising mud fluids that lack buffering by quartz-rich lithologies of the decending slab.

6. Conclusions

Observations on microfabric, petrography and trace element contents of serpentinized ultramafic clasts from South Chamorro Seamount provide novel insights into the prevailing conditions in the shallow mantle beneath the Mariana forearc. Detailed analyses of phase relations (low-temperature serpentine polymorphs lizardite and chrysotile, absence of antigorite and magnetite) and mineral chemistry of the successive serpentine generations present in the clasts, as well as oxygen isotope data, reveal low-temperature conditions ($\leq$ 250 ℃), as proposed by thermal models of cold oceanic subduction zones. Correlation of trace element concentrations and ratios in serpentine from clasts and mud matrix with either mud-volcano pore water analyses or experimental investigations of trace element mobilization reveal fluids derived from sediments at low temperatures as potential source of the serpentinizing fluids.

The rheological properties of suprasubduction mantle material in a cold oceanic subduction zone pose distinct boundary conditions on the serpentinization

942 processes: (i) convection is absent in the tapering mantle wedge above the

943 decoupling-coupling transition; (ii) within the wedge, and likely on the interface

944 between subducting slab and overlying mantle, lizardite is capable of a strain

945 localization into sample-scale shear bands. Therefore, within the wedge, the passage

946 of fluids may be confined to fractures, which is the prerequisite for the transfer of

947 serpentinized bouyant material to rise from the slab-mantle interface via conduits to

948 the mounds of the mud volcanoes. Moreover, due to the characteristic mechanical

949 properties of the low-temperature serpentine phases, partly serpentinized mantle

950 material can be eroded at shallow levels of the decollement from the basal interface

951 downward in the subduction channel, and still preserve fabric records and chemical

952 signatures of the early stages of serpentinization.

953

954 High concentrations of fluid mobile elements in the early stages of the polyphase

955 serpentinization history of the clasts, in contrast to FME-poor serpentine present in

956 the late vein generations in these clasts and also in the mud matrix serpentine point

957 to a change in the nature of the serpentinizing fluids throughout the history of

958 serpentinization and eruption. We propose, that the continued microfabric and

959 mineral chemical evolution observed in the ultramafic clasts is consistent with (1) the

960 partial serpentinization and erosion of mantle material off the basal plane of the

961 suprasubduction mantle wedge in shallower parts of the decollement, (2) the

962 subsequent descent in the subduction channel to the depth beneath South Chamorro

963 Seamount, and (3) the rise as clasts through the conduit towards the mound of the

964 mud volcano.

965

966 Sediments seem to play a vital role not only in the explanation of the observed trace

967 element ratios in the actual samples, but potentially also for the generation of fluids

968 under low-T conditions, and thus promoting the formation of mud volcanos in forearc

969 regions of nonaccretionary cold subduction zones. With this respect, additional

970 experimental data on the mobilization of FME from sediments are essential,
971 especially on the partition coefficients of these with the different serpentine
972 polymorphs. Moreover, research on the occurrence of certain serpentine polymorphs
973 in different serpentinization microfabrics may allow for more detailed mass (and
974 volume) balanced estimations. This will further the understanding of how subduction-
975 zone processes are connected to the hydration of ultramafic rocks.

976

977

978

987

988

989 **References**

990 Alt, J.C., Shanks III, W.C., 2006. Stable isotope compositions of serpentinite
991 seamounts in the Mariana forearc: serpentinization processes, fluid sources and
992 sulphur metasomatism. Earth and Planetary Science Letters 242, 272-285.

993

994 Alt, J. C., Laverne, C., Coggon, R.M., Teagle, D.A.H., Banerjee, N.R., Morgan, S.,
995 Smith‑Duque, C.E., Harris, M., Galli, L., 2010. Subsurface structure of a submarine

996 hydrothermal system in ocean crust formed at the East Pacific Rise, ODP/IODP Site

997 1256. Geochemistry, Geophysics, Geosystems 11, Q10010.

998

999 Andreani, M., Baronnet, A., Boullier, A.-M., Gratier, J.-P., 2004. A microstructural

1000 study of a crack-seal type serpentine vein, using SEM and TEM techniques.

1001 European Journal of Mineralogy 16, 585-595.

1002

1003 Andreani, M., Mével, C., Boullier, A.-M., Escartin, J., 2007. Dynamic control on

1004 serpentine crystallization in veins: constraints on hydration processes in oceanic

1005 peridotites. Geochemistry, Geophysics, Geosystems 8, Q02012.

1006

1007 Andreani, M., Muñoz, M., Marcaillou, C., Delacour, A., 2013. μ XANES study of iron

1008 redox state in serpentine during oceanic serpentinization. Lithos 178, 70-83.

1009

1010 Armstrong, J.T., 1995. CITZAF: A package of correction programs for the

1011 quantitative electron microbeam X-ray analysis of thick polished materials, thin films,

1012 and particles. Microbeam Analysis 4, 177-200.

1013

1014 Auzende, A.-L., Daniel, I., Reynard, B., Lemaire, C., Guyot, F., 2004. High-pressure

1015 behaviour of serpentine minerals: a Raman spectroscopic study. Physics and

1016 Chemistry of Minerals 31, 269-277.

1017

1018 Bach, W., Paulick, H., Garrido, C. J., Ildefonse, B., Meurer, W.P., and Humphris, S.

1019 E., 2006. Unraveling the sequence of serpentinitzation reactions: petrography,

1020 mineral chemistry, and petrophyscis of serpentinites from MAR 15ºN (ODP Leg 209,

1021 Site 1274). Geophysical Research Letters 33, L13306.

1022

1023 Beard, J.S., Frost, B.R., Fryer, P., McCaig, A., Searle, R., Ildefonse, B., Zinin, P.,

1024 Sharma, S.K., 2009. Onset and progression of serpentinization and magnetite

1025 formation in olivine-rich troctolite from IODP Hole U1309D. Journal of Petrology 50,

1026 387-403.

1027

1028 Bebout, G.E., Bebout, A.E., Graham, C.M., 2007. Cycling of B, Li, and LILE (K, Cs,

1029 Rb, Ba, Sr) into subduction zones: SIMS evidence from micas in high-P/T

1030 metasedimentary rocks. Chemical Geology 239, 284-304.

1031

1032 Bebout, G.E., 2007. Metamorphic chemical geodynamics of subduction zones. Earth

1033 and Planetary Science Letters 260, 373-393.

1034

1035 Becker, J.J., Sandwell, D.T., Smith, W.H.F., Braud, J., Binder, B., Depner, J., Fabre,

1036 D., Factor, J., Ingalls, S., Kim, S.-H., Ladner, R., Marks, K., Nelson, S., Pharaoh, A.,

1037 Trimmer, R., von Rosenberg, J., Wallace, G., Weatherall, P., 2009. Global

1038 bathymetry and elevation data at 30 Arc seconds resolution: SRTM30_PLUS. Marine

1039 Geodesy 32, 355-371.

1040

1041 Benton, L.D., Ryan J.G., Tera, F., 2001. Boron isotope systematics of slab fluids as

1042 inferred from a serpentine seamount, Mariana forearc. Earth and Planetary Science

1043 Letters 187, 273-82.

1044

1045 Bloomer, S.H., 1983. Distribution and origin of igneous rocks from the landward

1046 slopes of the Mariana Trench: implications for its structure and evolution. Journal of

1047 Geophysical Research 88, 7411-28.

1048

1049 Bonatti, E., Michael, P.J., 1989. Mantle peridotites from continental rifts to ocean

1050 basins to subduction zones. Earth and Planetary Science Letters 91, 297-311.

1051

1052   Bons, P.D., Elburg, M.A., Gomez-Rivas, E., 2012. A review of the formation of

1053   tectonic veins and their microstructures. Journal of Structural Geology 43, 33-62.

1054

1055   Boudier, F., Baronnet, A., Mainprice, D., 2010. Serpentine mineral replacements of

1056   natural olivine and their seismic implications: Oceanic lizardite versus subduction-

1057   related antigorite. Journal of Petrology 51, 495-512.

1058

1059   Clayton, R.N., Mayeda, T.K., 1963. The use of bromine pentafluoride in the

1060   extraction of oxygen from oxides and silicates for isotopic analysis. Geochimica

1061   Cosmochimica Acta 27, 43-52.

1062

1063   Cloos, M., Shreve, R.L., 1988a. Subduction-channel model of prism accretion,

1064   melange formation, sediment subduction, and subduction erosion at convergent plate

1065   margins; Part I, background and description. Pure and Applied Geophysics 128, 455-

1066   500.

1067

1068   Cloos, M., Shreve, R.L., 1988b. Subduction-channel model of prism accretion,

1069   melange formation, sediment subduction, and subduction erosion at convergent plate

1070   margins; Part II, implications and discussion. Pure and Applied Geophysics 128, 501-

1071   545.

1072

1073   D'Antonio, M., Kristensen, M.B., 2004. Serpentine and brucite of ultramafic clasts

1074   from the South Chamorro Seamount (Ocean Drilling Program Leg 195, Site 1200):

1075   Inferences for the serpentinization of the Mariana forearc mantle. Mineralogical

1076   Magazine 68, 887-904.

1077

1078   Deschamps, F., Guillot, S., Godard, M., Chauvel, C., Andreani, M., Hattori, K., 2010.

1079   In situ characterization of serpentinites from forearc mantle wedges: timing of

1080   serpentinization and behavior of fluid-mobile elements in subduction zones.

1081   Chemical Geology 269, 262-277.

1082

1083   Deschamps, F., Guillot, S., Godard, M., Andreani, M., Hattori, K., 2011. Serpentinites

1084   act as sponges for fluid-mobile elements in abyssal and subduction zone environ-

1085   ments. Terra Nova 23, 171-178.

1086

1087   Dilek, Y., Coulton, A.J., Hurst, S.D., 1997. Serpentinization and hydrothermal veining

1088   in peridotites at site 920 in the Mark area. Proceedings of the Ocean Drilling

1089   Program, Scientific Results 153, pp. 35-59.

1090

1091   Escartín, J., Hirth, G., B. Evans, B., 1997. Effects of serpentinization on the

1092   lithospheric strength and the style of normal faulting at slow-spreading ridges. Earth

1093   and Planetary Science Letters 151, 181-189.

1094

1095   Evans, B.W., 2004. The serpentine multisystem revisited: chrysotile is metastable.

1096   International Geology Review, 46, 479-506.

1097

1098   Fryer, P., 1992. A synthesis of Leg 125 drilling of serpentine seamounts on the

1099   Mariana and Izu-Bonin forearcs. In: Dearmont, L.H., Mazzullo, E.K., Stewart, N.J.,

1100   Winkler, W.R., (Eds.), Proceedings of the Ocean Drilling Program, Scientific Results,

1101   125, pp. 593-614.

1102

1103   Fryer, P., 1996. Evolution of the Mariana Convergent Plate Margin System. Reviews

1104   of Geophysics 34(1), 89-125.

1105

1106 Fryer, P., Ambos, E.L., Hussong, D.M., 1985. Origin and emplacement of Mariana

1107 forearc seamounts. Geology 13, 774-777.

1108

1109 Fryer, P., Fryer, G.J., 1987. Origin of non-volcanic seamounts in a forearc

1110 environment. Seamounts, Islands and Atolls: In: Keating, B., Fryer, P., Batiza, R.

1111 (Eds.), A.G.U. Geophysical Monograph, 43, pp. 61-69.

1112

1113 Fryer, P., Pearce, Julian A., Stokking, Laura B., et al., 1990. Bonin/Mariana region,

1114 covering Leg 125 of the cruises of the drilling vessel JOIDES Resolution, Apra

1115 Harbor, Guam, to Tokyo, Japan, sites 778–786. In: Fryer, P., Pearce, J.A., Stokking,

1116 L.B., et al. (Eds.), Proceedings of the Ocean Drilling Program Initial Reports, 125, pp.

1117 367-380.

1118

1119 Fryer, P., Wheat, C.G., Mottl, M.J., 1999. Mariana Blueschist mud volcanism:

1120 implications for conditions within the subduction zone. Geology 27, 103-106.

1121

1122 Fryer, P., Lockwood, J., Becker, N., Todd, C., Phipps, S., 2000. Significance of

1123 serpen- tine and blueschist mud volcanism in convergent margin settings. In: Dilek,

1124 Y., et al. (Ed.), Ophiolites and Oceanic Crust: New Insights from Field Studies and

1125 Ocean Drilling Program: Special Papers Geological Society of America, 349, pp. 35-

1126 51.

1127

1128 Fryer, P., Salisbury, M.H., 2006. Leg 195 synthesis: site 1200 - serpentinite

1129 seamounts of the Izu Bonin/Mariana convergent plate margin (ODP Leg 125 and 195

1130 drilling results). In: Shinohara, M., Salisbury, M.H., Richter, C. (Eds.), Proceedings of

1131 the Ocean Drilling Program, Scientific Results, 195, pp. 1-30.

1132

1133   Furukawa, Y., 1993. Depth of the decoupling plate interface and thermal structure

1134   under arcs. Journal of Geophysical Research 98, 20,005-20,013.

1135

1136   Godard, M., Luquot, L., Andreani, M., Gouze, P., 2013. Incipient hydration of mantle

1137   lithosphere at ridges: A reactive-percolation experiment. Earth and Planetary Science

1138   Letters 371-372, 92-102.

1139

1140   Groppo, C., Rinaudo, C., Cairo, S., Gastaldi, D., Compagnoni, R., 2006. Micro-

1141   Raman spectroscopy for a quick and reliable identification of serpentine minerals

1142   from ultramafics. European Journal of Mineralogy 18, 319-329.

1143

1144   Hirauchi, K., Katayama, I., Uehara, S., Miyahara, M., Takai, Y., 2010. Inhabitation of

1145   subduction thrust earthquakes by low-temperature plastic flow in serpentine. Earth

1146   and Planetary Science Letters 295, 349-357.

1147

1148   Hulme, S., Wheat, C.G., Fryer, P., Mottl, M.J., 2010. Pore-water chemistry of the

1149   Mariana serpentinite mud volcanoes: a window to the seismogenic zone.

1150   Geochemistry, Geophysics, Geosystems 11, Q01X09.

1151

1152   Hyndman, R.D., Peacock, S.M., 2003. Serpentinization of the forearc mantle. Earth

1153   and Planetary Science Letters 212, 417-432.

1154

1155   Ishii, T., Robinson, P.T., Maekawa, H., Fiske, R., 1992. Petrological studies of

1156   peridotites from diapiric serpentinite seamounts in the Izu-Ogasawara-Mariana

1157   forearc, Leg 125. In: Fryer, P., Pearce, J.A., Stokking, L.B., et al. (Eds.), Proceedings

1158   of the Ocean Drilling Program, Scientific Results, 125, pp. 445-485.

1159

1160   Iyer, K., Austrheim, H., John, T., Jamtveit, B., 2008a. Serpentinization of the oceanic

1161   lithosphere and some geochemical consequences: constraints from the Leka

1162   Ophiolite complex, Norway. Chemical Geology 249(1-2), 66-90.

1163

1164   Iyer, K., Jamtveit, B., Mathiesen, J., Malthe-Sorenssen, A., Feder, J., 2008b.

1165   Reaction-assisted hierarchical fracturing during serpentinization. Earth and Planetary

1166   Science Letters 267(3-4), 503-516.

1167

1168   Jochum, K. P., Weis, U., Stoll, B., Kuzmin, D., Yang, Q., Raczek, I., Jacob, D. E.,

1169   Stracke, A., Birbaum, K., Frick, D. A., Günther, D., Enzweiler, J., 2011. Determination

1170   of Reference Values for NIST SRM 610-617 Glasses Following ISO Guidelines.

1171   Geostandards and Geoanalytical Research 35, 397-429.

1172

1173   Jochum, K.P., Stoll, B., Herwig, K., Willbold, M., Hofmann, A.W., Amini, M., Aarburg,

1174   S., Abouchami, W., Hellebrand, E., Mocek, B., Raczek, I., Stracke, A., Alard, O.,

1175   Bouman, C., Becker, S., Dücking, M., Brätz, H., Klemd, R., de Bruin, D., Canil, D.,

1176   Cornell, D., de Hoog, C.-J., Dalpé, C., Danyushevsky, L., Eisenhauer, A., Gao, Y.,

1177   Snow, J.E., Groschopf, N., Günther, D., Latkoczy, C., Guillong, M., Hauri, E.H.,

1178   Höfer, H.E., Lahaye, Y., Horz, K., Jacob, D.E., Kasemann, S.A., Kent, A.J.R.,

1179   Ludwig, T., Zack, T., Mason, P.R.D., Meixner, A., Rosner, M., Misawa, K., Nash,

1180   B.P., Pfänder, J., Premo, W.R., Sun, W.D., Tiepolo, M., Vannucci, R., Vennemann,

1181   T., Wayne, D., Woodhead, J.D., 2006. MPI-DING reference glasses for in situ

1182   microanalysis: new reference values for element concentrations and isotope ratios.

1183   Geochemistry, Geophysics, Geosystems 7, Q02008.

1184

1185   Katayama, I., 2009. Thin anisotropic layer in the mantle wedge beneath northeast

1186   Japan. Geology 37, 211-214.

1187

1188 Klein, F., Bach, W., Jöns, N., McCollom, T., Moskowitz, B., Berquó, T., 2009. Iron

1189 partitioning and hydrogen generation during serpentinization of abyssal peridotites

1190 from 15°N on the Mid-Atlantic Ridge. Geochimica et Cosmochimica Acta 73, 6868-

1191 6893.

1192

1193 Klein, F., Bach, W., Humphris, S. E., Kahl, W.-A., Jöns, N., Moskowitz, B., Berquó,

1194 T., 2014. Magnetite in seafloor serpentinite - Some like it hot. Geology 42(2), 135-

1195 138.

1196

1197 Kodolanyi, J., Pettke, T., Spandler, C., Kamber, B.S., Gmeling, K., 2012.

1198 Geochemistry of ocean floor and fore-arc serpentinites: Constraints on the ultramafic

1199 input to subduction zones. Journal of Petrology 53, 235-270.

1200

1201 Lafay, R., Montes-Hernandez, G., Janots, E., Chiriac, R., Findling, N., Toche, F.,

1202 2012. Mineral replacement rate of olivine by chrysotile and brucite under high

1203 alkaline conditions. Journal of Crystal Growth 347, 62-72.

1204

1205 Lawrence, J.R., Drever, J.L., 1981. Evidence for cold water circulation at DSDP Site

1206 395: isotopes and chemistry of alteration products. Journal of Geophysical Research

1207 86, 5125-5133.

1208

1209 Meffre, S., Falloon, T.J., Crawford, T.J., Hoernle, K., Hauff, F., Duncan, R.A.,

1210 Bloomer, S.H., Wright, D.J., 2012. Basalts erupted along the Tongan fore arc during

1211 subduction initiation: Evidence from geochronology of dredged rocks from the Tonga

1212 fore arc and trench. Geochemistry, Geophysics, Geosystems 13, Q12003.

1213

1214   Mellini, M., Rumori, C., Viti, C., 2005. Hydrothermally reset magmatic spinels in

1215   retrograde serpentinites, formation of "ferritchromit" rims and chlorite aureoles.

1216   Contributions to Mineralogy and Petrology 149, 266-275.

1217

1218   Michibayashi, K., Tasaka, M., Ohara, Y., Ishii, T., Okamoto, A., Fryer, P., 2007.

1219   Variable microstructure of peridotite samples from the southern Mariana Trench:

1220   evidence of a complex tectonic evolution. Tectonophysics 444, 111-118.

1221

1222   Moore, J.C., Saffer, D., 2001. Updip limit of the seismogenic zone beneath the

1223   accretionary prism of southwest Japan: An effect of diagenetic to low-grade

1224   metamorphic processes and increasing effective stress. Geology 29(2), 183–186.

1225

1226   Mottl, M.J., 1992. Pore waters from serpentine seamounts in the Mariana and Izu-

1227   Bonin forearcs, Leg 125: evidence for volatiles from the subducting slab. In: Fryer,

1228   P., Pearce, J.A., Stokking, L.B., et al. (Eds.), Proceedings of the Ocean Drilling

1229   Program, Scientific Results, 125, pp. 373-385.

1230

1231   Mottl, M.J., Komor, S.C., Fryer, P. Moyer, C.L., 2003. Deep-slab fluids fuel

1232   extremophilic Archaea on a Mariana forearc serpentinite mud volcano: Ocean Drilling

1233   Program Leg 195. Geochemistry Geophysics and Geosystems 4(11), 9009.

1234

1235   Mottl, M.J., Wheat, C.G., Fryer, P., Gharib, J., Martin, J.B., 2004. Chemistry of

1236   springs across the Mariana forearc shows progressive devolatilization of the

1237   subducting plate. Geochimica et Cosmochimica Acta 68(23), 4915-4933.

1238

1239   Murata, K., Maekawa, H., Yokose, H., Yamamoto, K., Fujioka, K., Ishii, T., Chiba, H.,

1240   Wada, Y., 2009. Significance of serpentinization of wedge mantle peridotites beneath

1241   Mariana forearc, western Pacific. Geosphere, 5, 90-104.

1242

1243   Oakley, A.J., Taylor, B., Fryer, P., Moore, G.F., Goodliffe, A.M., Morgan, J.K., 2007.

1244   Emplacement, growth, and gravitational deformation of serpentinite seamounts on

1245   the Mariana forearc, Geophysical Journal International 170(2), 615-634.

1246

1247   O'Hanley, D.S. (1996) Serpentinites: Record of Tectonic and Petrologic History. New

1248   York: Oxford University Press.

1249

1250   Pabst, S., Zack, T., Savov, I.P., Ludwig, T., Rost, D., Vicenzi, E.P., 2011. Evidence

1251   for boron incorporation into the serpentine crystal structure. American Mineralogist,

1252   96, 1112-1119.

1253

1254   Pabst, S., 2009. Investigation of blueschist and serpentinized harzburgite from the

1255   Mariana forearc: Insights into the mechanisms of element mobilization in subduction

1256   zones and storage of fluid-mobile elements in the mantle wedge. PhD Dissertation,

1257   Heidelberg, Germany. http://www.ub.uni-heidelberg.de/archiv/10181.

1258

1259   Parkinson, I.J., Pearce, J.A., 1998. Peridotites from the Izu-Bonin-Mariana forearc

1260   (ODP Leg 125), Evidence for mantle melting and melt-mantle interaction in a supra-

1261   subduction zone setting. Journal of Petrology 39, 1577-1618.

1262

1263   Pearce, J.A., Baker, P.F., Edwards, S.J., Parkinson, I.J., Leat, P.T., 2000.

1264   Geochemistry and tectonic significance of peridotites from the South-Sandwich arc-

1265   basin system, South Atlantic. Contributions to Mineralogy and Petrology 139, 36-53.

1266

1267   Plank, T., Langmuir, C., 1998. The chemical composition of subducting sediment and

1268   its consequences for the crust and mantle. Chemical Geology 145, 325-394.

1269

1270   Plümper, O., Røyne, A., Magrasó, A., Jamtveit, B., 2012. The interface-scale

1271   mechanism of reaction-induced fracturing during serpentinization. Geology 40, 1103-

1272   1106.

1273

1274   Reynard, B., 2013. Serpentine in active subduction zones. Lithos 178, 15, 171-185.

1275

1276   Rinaudo, C., Gastaldi, D., Belluso, E., 2003. Characterization of chrysotile, antigorite

1277   and lizardite by FT-Raman spectroscopy. Canadian Mineralogist 41, 883-890.

1278

1279   Rüpke, L.H., Morgan, J.P., Hort, M., Connolly, J.A.D., 2002. Are the regional

1280   variations in Central American arc lavas due to differing basaltic versus peridotitic

1281   slab sources of fluids? Geology 30, 1035-1038.

1282

1283   Rüpke, L.H., Morgan, J.P., Hort, M., Connolly, J.A.D., 2004. Serpentine and the

1284   subduction zone water cycle. Earth and Planetary Science Letters 223, 17-34.

1285

1286   Sakai, R., Kusakabe, M., Noto, M., Ishii, T., 1990. Origin of waters responsible for

1287   serpentinization of the Izu-Ogasawara-Mariana forearc seamounts in view of

1288   hydrogen and oxygen isotope ratios. Earth and Planetary Science Letters 100(1-3),

1289   291-303.

1290

1291   Saboda, K.L., Fryer, P., Maekawa, H., 1992. Metamorphism of ultramafic clasts from

1292   Conical Seamount: sites 778, 779, and 780. In: Fryer, P., Pearce, J.A., Stokking,

1293   L.B., et al. (Eds.), Proceedings of the Ocean Drilling Program, Scientific Results, 125,

1294   pp. 373-385. pp. 431-444.

1295

1296   Salisbury, M.H., Shinohara, M., Richter, C., Araki, E., Barr, S.R., D'Antonio, M.,

1297   Dean, S.M., Diekmann, B., Edwards, K.M., Fryer, P.B., Gaillot, P.J., Hammon III,

1298   W.S., Hart, D., Januszczak, N., Komor, S.C., Kristensen, M.B., Lockwood, J.P.,

1299   Mottl, M.J., Moyer, C.L., Nakahigashi, K., Savov, I.P., Su, X., Wei, K.-Y., Yamada, T.,

1300   2002. Proceeding of the Ocean Drilling Program, Initial Reports, 195.

1301

1302   Saumur, B.M., Hattori, K., 2013. Zoned Cr-spinel and ferritchromite alteration in

1303   forearc mantle serpentinites of the Rio San Juan Complex, Dominican Republic.

1304   Mineralogical Magazine 77 (1), 117–136.

1305

1306   Savov, I.P., Guggino, S., Ryan, J.G., Fryer, P., Mottl, M.J., 2005a. Geochemistry of

1307   serpentinite muds and metamorphic rocks from the Mariana forearc, ODP Sites 1200

1308   and 778–779, South Chamorro and Conical Seamounts. In: Shinohara, M.,

1309   Salisbury, M.H., Richter, C. (Eds.), Proceedings of the Ocean Drilling Program,

1310   Scientific Results, 195.

1311

1312   Savov, I.P., Ryan, J.G., D'Antonio, M., Kelley, K., Mattie, P., 2005b. Geochemistry of

1313   ser- pentinized peridotites from the Mariana Forearc Conical Seamount, ODP Leg

1314   125: Implications for the elemental recycling at subduction zones. Geochemistry,

1315   Geophysics, Geosystems 6.

1316

1317   Savov, I.P., Ryan, J.G., D'Antonio, M., Fryer, P., 2007. Shallow slab fluid release

1318   across and along the Mariana arc-basin system: Insights from geochemistry of

1319   serpentinized peridotites from the Mariana fore arc. Journal of Geophysical

1320   Research-Solid Earth 112, B09205.

1321

1322   Schmidt, M.W., Poli, S., 1998. Experimentally based water budgets for dehydrating

1323   slabs and consequences for arc magma generation. Earth and Planetary Science

1324   Letters 163, 361-379.

1325

1326   Schwartz, S., Guillot, S., Reynard, B., Lafay, R., Debret, B., Nicollet, C., Lanari, P.,

1327   Auzende, A. L., 2012. Pressure-temperature estimates of the lizardite/antigorite

1328   transition in high pressure serpentinites. Lithos 178, 197-210.

1329

1330   Seyfried, W.E.,Jr., Foustoukos, D.I., Fu, Q., 2007. Redox evolution and mass

1331   transfer during serpentinization: An experimental and theoretical study at 200°C, 500

1332   bar with implications for ultramafic-hosted hydrothermal systems at Mid-Ocean

1333   Ridges. Geochimica et Cosmochimica Acta 71, 3872-3886.

1334

1335   Seyler, M., Toplis, M.J., Lorand, J.P., Luguet, A., Cannat, M., 2001. Clinopyroxene

1336   microtextures reveal incompletely extracted melts in abyssal peridotites. Geology 29,

1337   155-158.

1338

1339   Snyder, G.T., Savov, I.P., Muramatsu, Y., 2005. Iodine and boron in Mariana

1340   serpentinite mud volcanoes (ODP Legs 125 and 195): implications for forearc

1341   processes and subduction recycling. In: Shinohara, M., Salisbury, M.H., Richter, C.

1342   (Eds.), Proceedings of the Ocean Drilling Program, Scientific Results, 195.

1343

1344   Spandler, C., Pirard, C., 2013. Element recycling from subducting slabs to arc crust:

1345   A review. Lithos 170-171, 208-223.

1346

1347   Straub, S.M., Layne, G.D., 2003. Decoupling of fluids and fluid-mobile elements

1348   during shallow subduction: evidence from halogen-rich andesite melt inclusions from

1349   the Izu arc volcanic front. Geochemistry, Geophysics, Geosystems 4.

1350

1351   Tibi, R., Wiens, D.A., Yuan, X., 2008. Seismic evidence for widespread serpentinized

1352   forearc mantle along the Mariana convergence margin. Geophysical Research

1353   Letters 35, L13303.

1354

1355   Wheat, C.G., Fryer, P., Fisher, A.T., Hulme, S., Jannasch, H., Mottl, M.J., Becker, K.,

1356   2008. Borehole observations of fluid flow from South Chamorro Seamount, an active

1357   serpentinite mud volcano in the Mariana forearc. Earth and Planetary Science Letters

1358   267, 401-409.

1359

1360   Wicks, F.J., Whittaker, E.J.W., 1977. Serpentine texture and serpentinization.

1361   Canadian Mineralogist 15, 459-488.

1362

1363   Wei, W., Kastner, M., Deyhle, A., Spivack, A.J., 2005. Geochemical cycling of

1364   fluorine, chlorine, bromine, and boron and implications for fluid-rock reactions in

1365   Mariana forearc, South Chamorro Seamount, ODP Leg 195. In: Shinohara, M.,

1366   Salisbury, M. H., Richter, C. (Eds.), Proceedings of the Ocean Drilling Program,

1367   Scientific Results, 195.

1368

1369   You, C.-F., Castillo, P.R., Gieskes, J.M., Chan, L.H., Spivack, A.J., 1996. Trace

1370   element behavior in hydrothermal experiments: implications for fluid processes at

1371   shallow depths in subduction zones. Earth and Planetary Science Letters 140, 41-52.

1372

Figure Captions

Fig. 1

(A) Bathymetric map of the Mariana arc-basin system showing the location of South

Chamorro Seamount, 85 km from the trench (Leg 195, Site 1200A). Regional map

prepared using GMT (Wessel and Smith, 1991). Elevation data from the

SRTM30_PLUS dataset (Becker et al., 2009). (B) Schematic diagram (no vertical

exaggeration) of the emplacement of serpentinite mud volcanoes on the outer

Mariana Forearc (modified from Oakley et al., 2007). The asterisk marks the relative

position of South Chamorro Seamount.

Fig. 2

Thin section photomicrographs of serpentinized ultramafic clasts documenting the

polyphase serpentinization history of the Mariana forearc mantle. (A) Sample 12R-1,

8-11 cm, showing early magnetite-bearing veins predating the pervasive stage,

developed linearly without marked conformance with the rock fabric. Back-scattered

electron image. (B) Expansional chrysotile type (ii) veins (brown) in sample 16R-2,

11-12 cm. Scanned thin section, plane-polarized light, image width 16 mm. (C)

Close-up of type (ii) veins in sample 16R-2, 7-9 cm, crossing pervasively

serpentinized harzburgite with relict olivine subgrains. Photomicrograph, cross-

polarized light, image width 1.7 mm. (D1 and D2) Type (iii) veins ("Frankenstein

veins"), developed in the halo of type (i) veins and crosscutting type (ii) veins in

sample 7R-2, 40-43 cm. Scanned thin section, plane- and cross-polarized,

respectively Image width D1 is 11 mm. (E) Type (iii) veins in the halo of type (i) veins

in sample 13R-2, 5-7 cm. Scanned thin section, cross-polarized light. Image height

10 mm. (F) Late-stage type (iv) veins of the multiple crack-seal type, indicating

clearly anisotropic expansion in sample 3R-1, 3-7 cm. Scanned thin section, plane-

polarized light, image width 10.5 mm. (G) Dunite sample 9R-1, 21-23 cm. Ribbons

contain submicroscopic intergrowth of serpentine and brucite. On the contrary, large,

1401 recrystallized brucite is observed in regions separated by the ribbons. Image height

1402 2.2 mm. (H) Samples 16R-1, 52-54 cm, and 16R-1, 62-64 cm, both from piece 11A,

1403 show browning, occuring from the clast's rim inward, which involves brucite formation

1404 in interstices. Scanned thin section, plane-polarized light. Image width 8 mm.

1405

1406 Fig. 3

1407 Detailed view of pervasive serpentinization fabrics. (A) and (B) Sample 7R-2, 40-43

1408 cm. Mesh textures developed in the forearc setting lack the formation of magnetite

1409 along mesh rims. Instead, awaruite and submicroscopic intergrowth of brucite and

1410 serpentine is observed. (C) and (D) Qualitative analyses of the same sample,

1411 indicating the absence of brucite rims around olivine cores.

1412

1413 Fig. 4

1414 Compositions of primary and secondary minerals of the different serpentinization

1415 events, plotted as molar proportions of Si-Mg-Fe in ternary diagrams. Primary

1416 minerals are given for orientation, they are not part of the assemblage. (A1) and (A2)

1417 Serpentine analyses of the pervasive stage in harzburgites and dunites. In dunites,

1418 the analyses low in Si are from recrystallized hourglass textures. (B) Analyses of

1419 serpentine-brucite phases from type (i) veins and the adjacent halo region. (C)

1420 Composition of serpentine-brucite, submicroscopically intergrown in expansional type

1421 (ii) veins in harzburgite. (D) Serpentine analyses of type (iii) and type (iv) veins,

1422 indicating anisotropic expansion in the course of the serpentinization process.

1423

1424 Fig. 5

1425 Variations of SiO_2, Al_2O_3, CaO and Cr_2O_3 content in primary and secondary minerals.

1426 (A) SiO_2 wt.% vs. Al_2O_3 wt.%. Serpentine grown after pyroxene shows Al_2O_3 as high

1427 as the precursor mineral, whereas serpentine grown in later events or after olivine

1428 shows low to intermediate Al contents. (B) In terms of CaO, bastites show similar

1429   contents as orthopyroxene. On the contrary, serpentine grown from olivine or during

1430   later events is enriched in Ca relative to olivine. (C) Cr_2O_3 content of bastites overlap

1431   with pyroxene Cr contents, whereas serpentine formed from olivine or during later

1432   events contains as low Cr as the primary olivine.

1433

1434   Fig. 6

1435   Trace element (Ni, V) - Si/(Mg+Fe) relationships in primary and secondary minerals.

1436   (A) Ni concentrations detected in serpentine-brucite intergrowth regions positively

1437   correlate with the serpentine fraction in the mixed analyses. (B) V is neither found in

1438   serpentine-brucite intergrowth regions, nor in type (ii) veins. (C) The Ni-V variation

1439   diagram shows the discriminatory significance for identifying the serpentine precursor

1440   mineral.

1441

1442

1443   Fig. 7

1444   Concentrations of B, Ba, Sr, Rb, and Cs in serpentine and serpentine-brucite mixed

1445   analyses. (A) to (E) Boron contents in general increase with increasing Srp-fraction in

1446   the mixed Srp-Brc analyses, showing medium to high B values both for early and late

1447   vein generations. Barium and Sr show high contents also in the type (ii) veins, but

1448   not in type (iii) and type (iv) late-stage veins. Cs and Rb exhibit marked enrichment in

1449   early serpentinization stages, and low contents in all types of late extensional veins.

1450   (F) Boron-Cs variation diagram, showing the overall high B contents of the

1451   serpentinization fluids of the various stages, in comparison to Cs in Srp, which

1452   exhibits markedly different concentrations throughout the serpentinization history.

1453

1454   Fig. 8

1455   Diagrams of (A) Cs vs. Rb, and (B) Sr vs. Ba in primary minerals and serpentine of

1456   the various serpentine generations. In both diagrams, fields of bulk rock analyses of

1457   1200A clasts and mud from Savov et al., (2007, and 2005a) are given. For

1458   comparison, Cs and Rb contents of forearc peridotites (Meffré et al., 2012), altered

1459   oceanic crust (Kelley et al., 2006), and of sediments (Plank and Langmuir, 1998) are

1460   shown. Furthermore, compositions of natural (Mottl et al., 2004) and experimental

1461   fluids and solids (Y-You et al., 1996) are plotted. See text for further discussion.

1462

1463   Fig. 9

1464   Relative chronology of the microfabric evolution, summarizing the observed fabric

1465   relations and generalized trace element concentrations of the polyphase

1466   serpentinization history of Mariana forearc mantle. (A) First serpentinization event

1467   along a discrete set of tiny fractures. (B) Phase of pervasive serpentinization under a

1468   static, isotropic pressure regime. (C) Phase of establishment of fluid pathways,

1469   generating focused fluid flow along type (i) veins. (D) Onset of anisotropic expansion

1470   features and occurrence of extensional type (ii) veins. (E) Formation of type (iii) veins

1471   in outer rock/clast (?) halo regions of type (i) veins to compensate continued

1472   expansion of the inner parts. (F) Multiple crack-seal veins of type (iv), located in the

1473   rim regions of the clasts.

1474

1475

1476 **Tables**

1477

1478 Table 1.

1479 Samples (clasts) from South Chamorro Smt., Leg 195, Site 1200A.

1480

1481 Table 2.

1482 Representative electron microprobe analyses and in situ LA-ICP-MS data of relict

1483 primary minerals from Leg 195, Site 1200A, South Chamorro Smt.

1484

1485 Table 3.

1486 Representative electron microprobe analyses and in situ LA-ICP-MS data of

1487 serpentinization products from Leg 195, Site 1200A, South Chamorro Smt.

1488

1489 Table 4.

1490 Overview of selected properties of serpentine from different serpentinization events.

1491

1492 Table 5.

1493 Oxygen isotope data of serpentinization products from different serpentinization

1494 phases in ultramafic clasts from South Chamorro Smt., Leg 195, Site 1200A.

modified after Oakley et al., (2007)
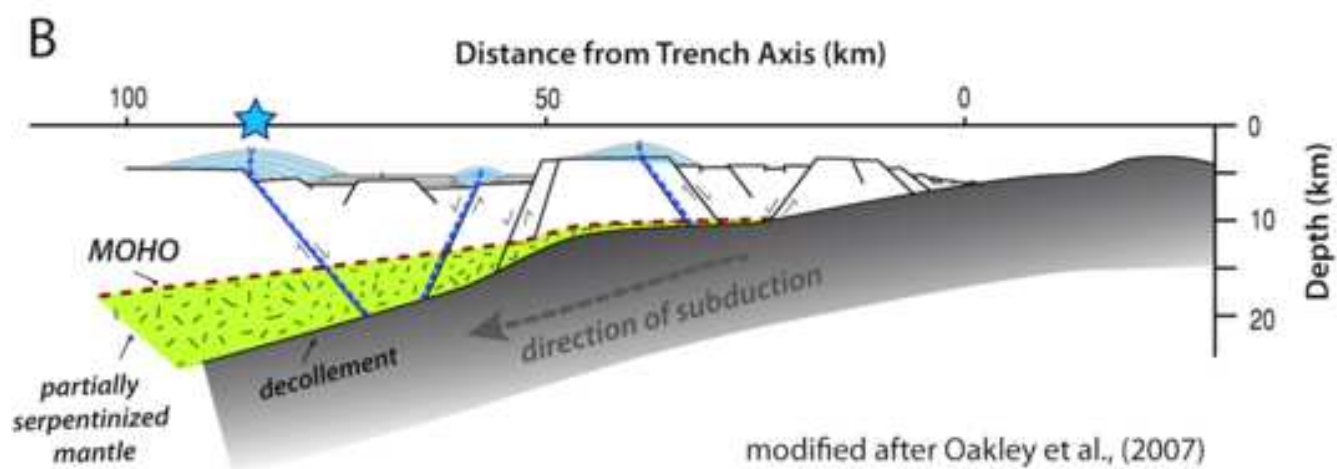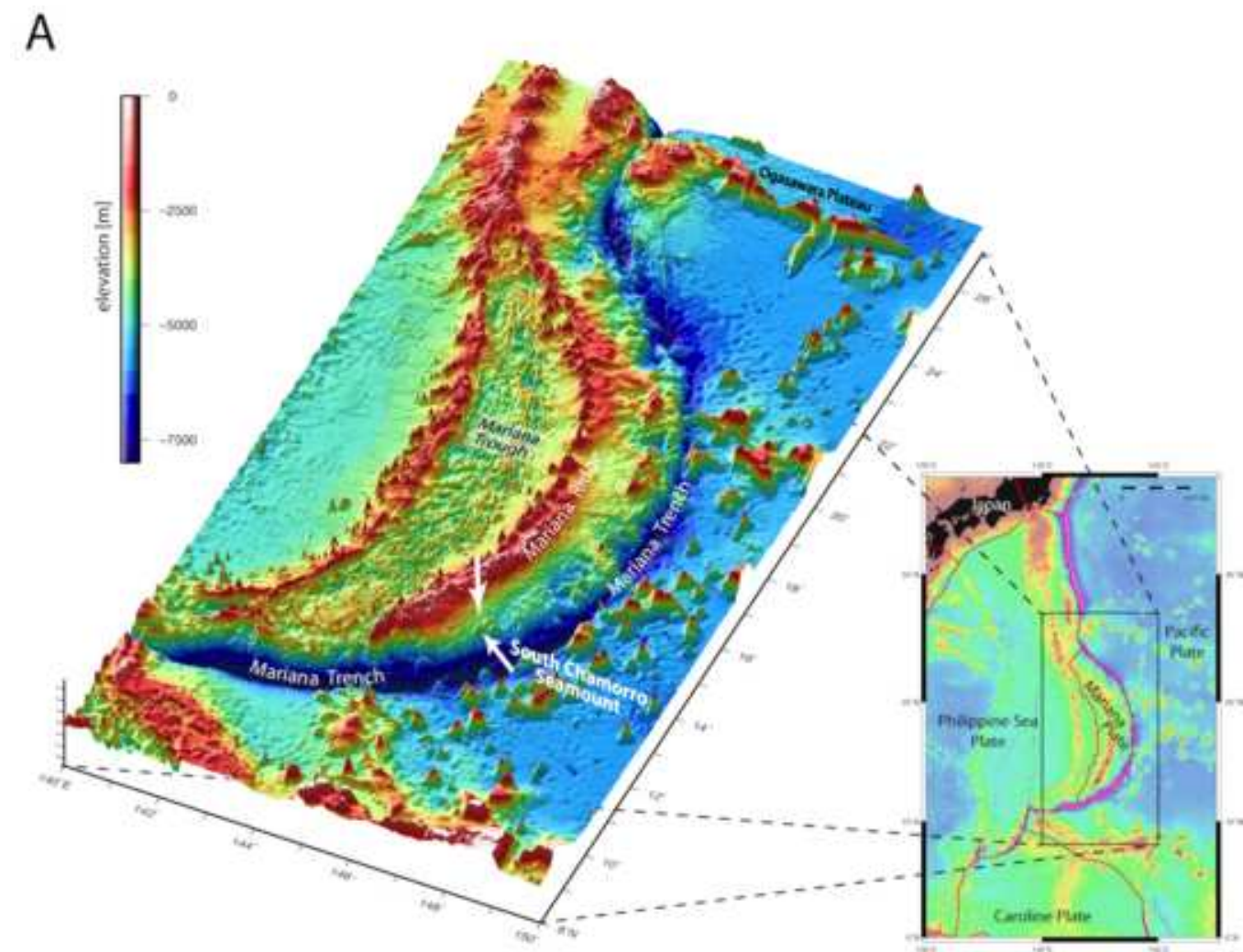
Figure2
Click here to download high resolution image
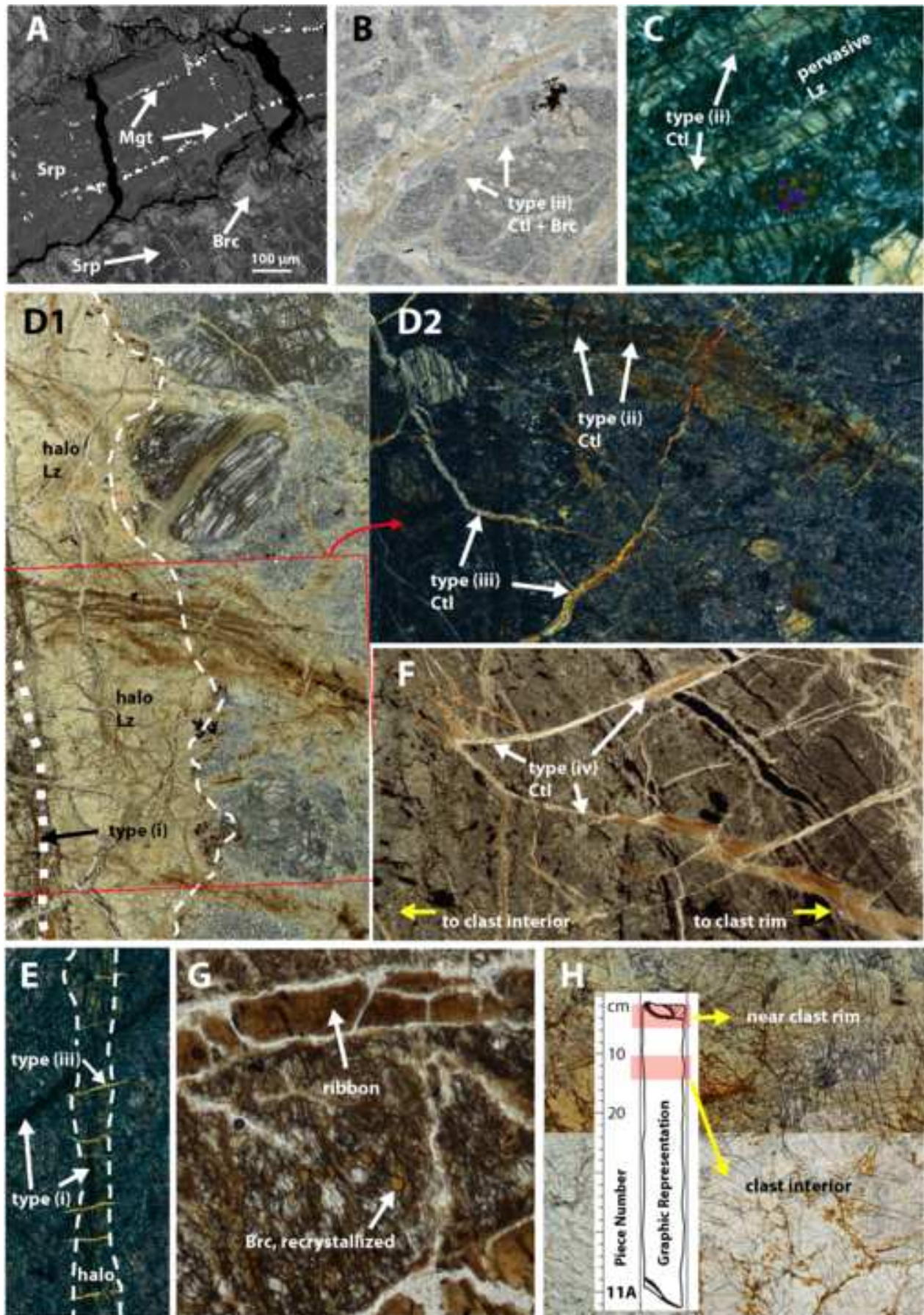
Figure3
Click here to download high resolution image
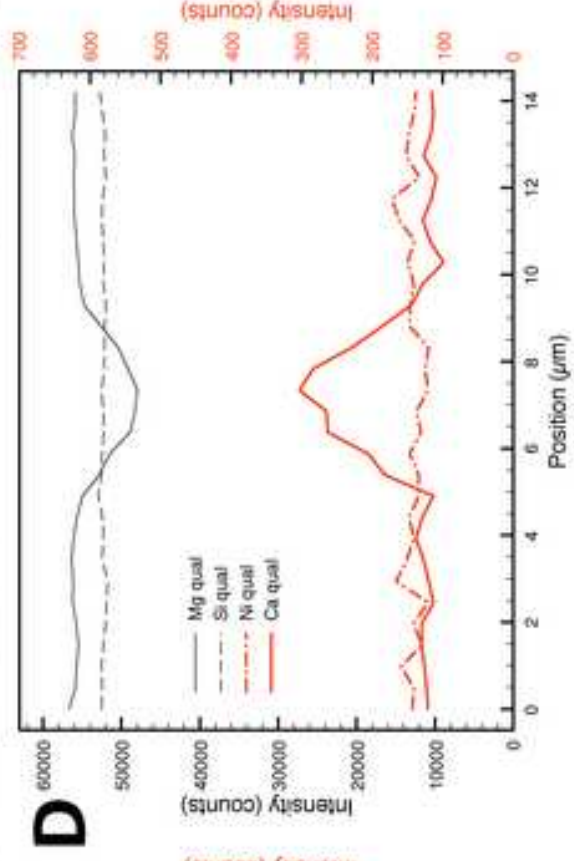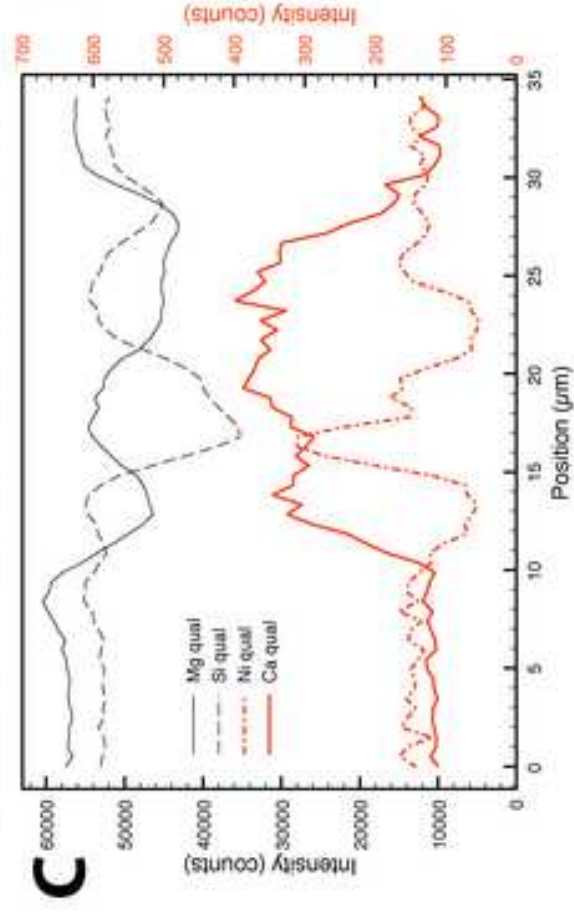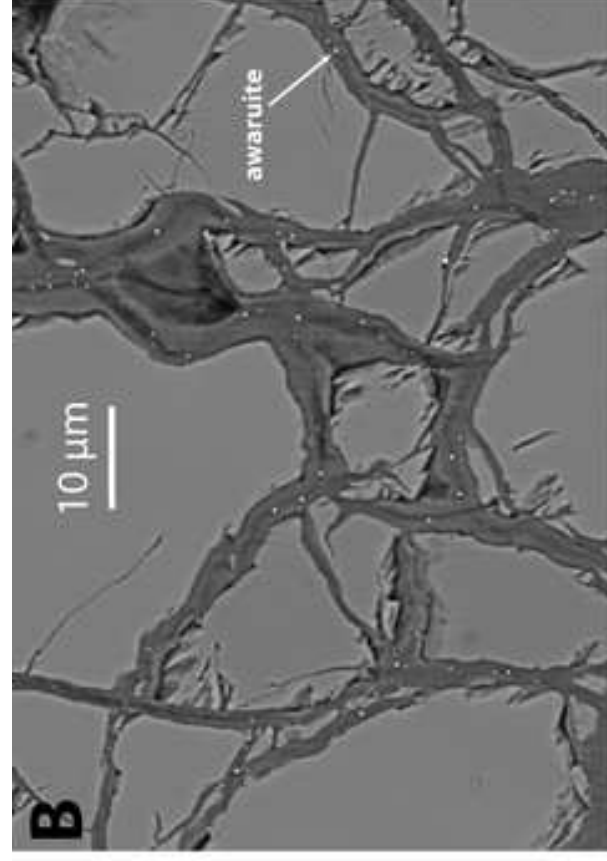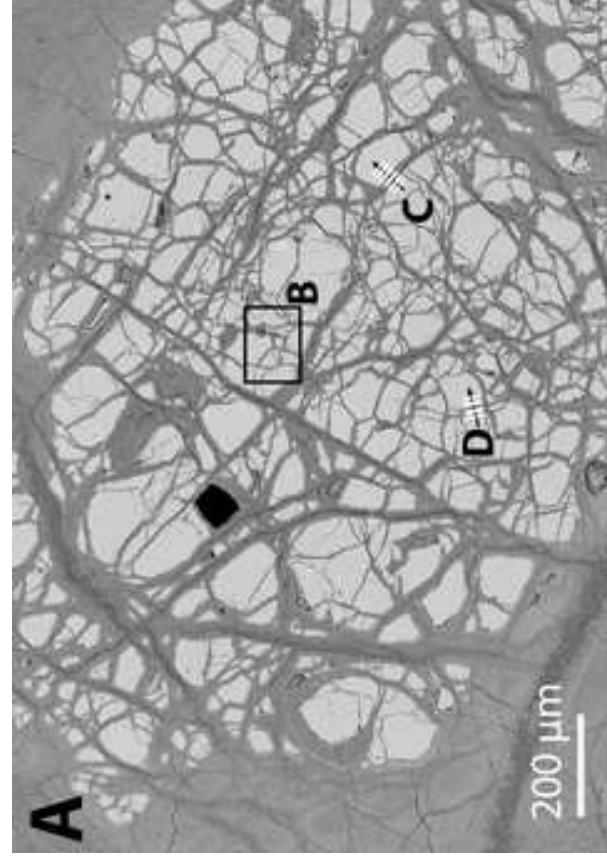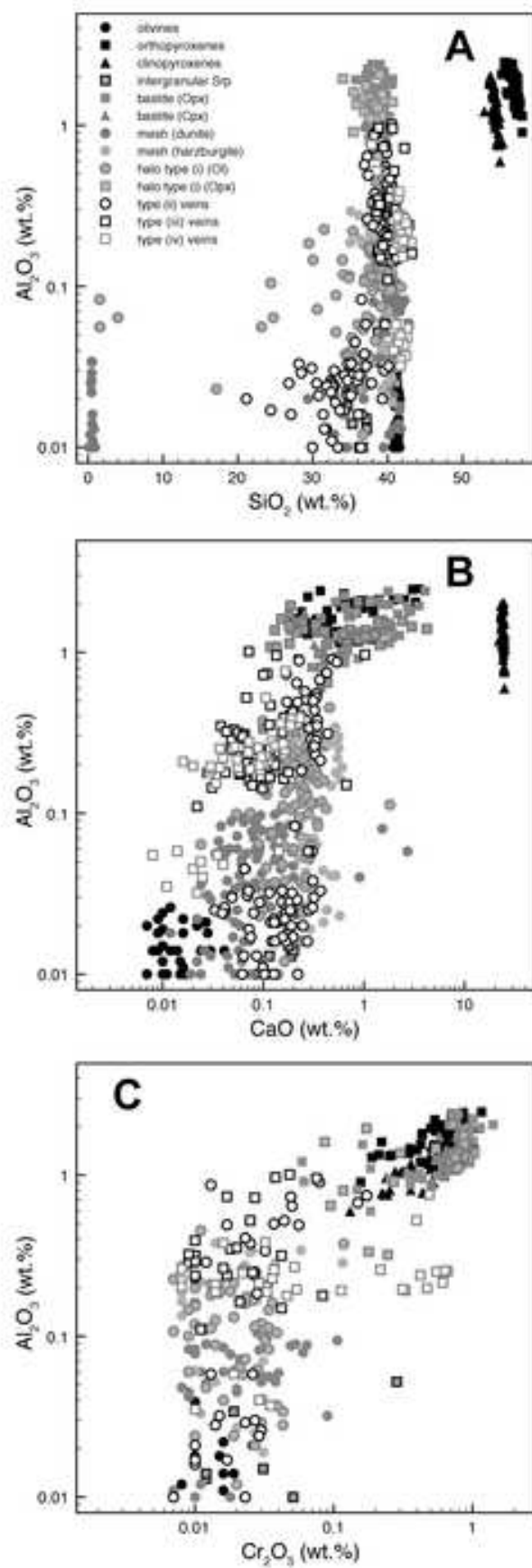
Figure6
Click here to download high resolution image
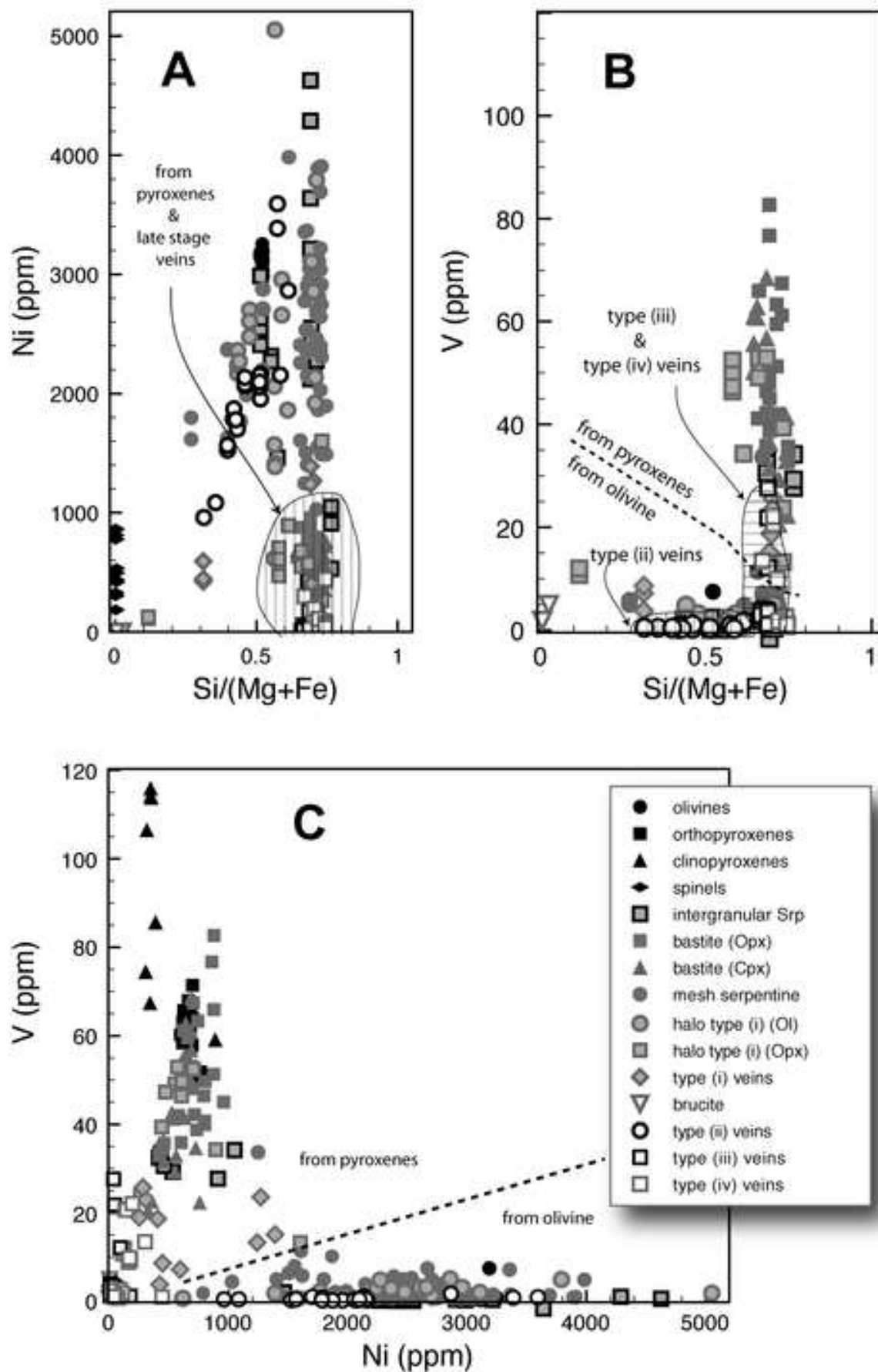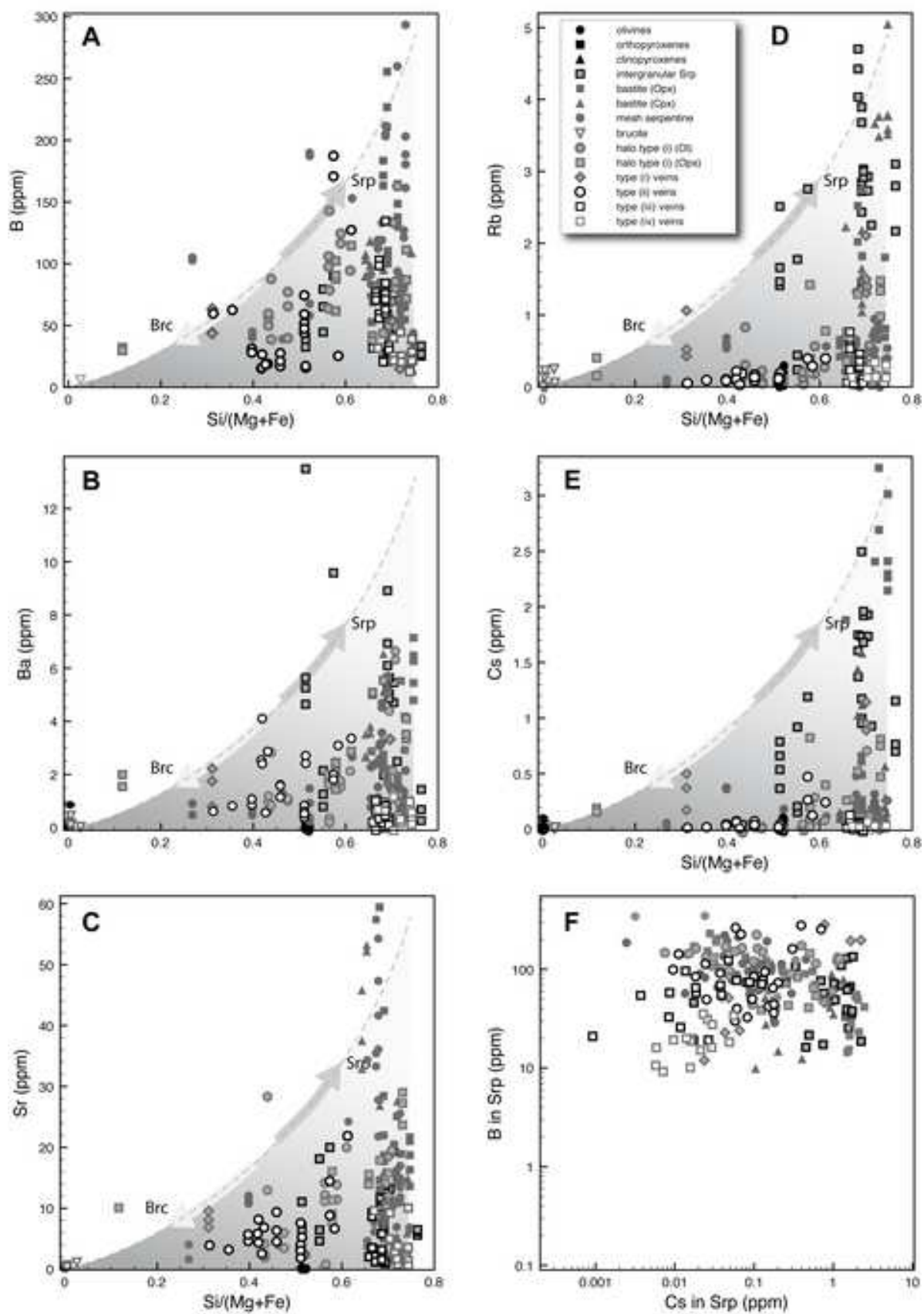
Figure8
Click here to download high resolution image
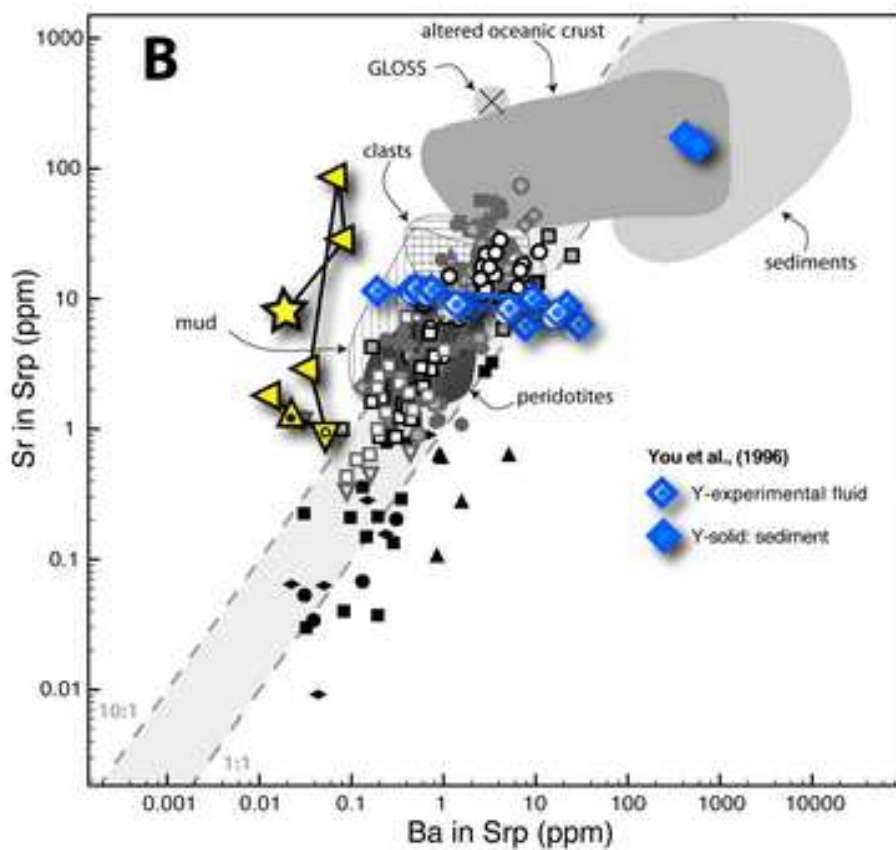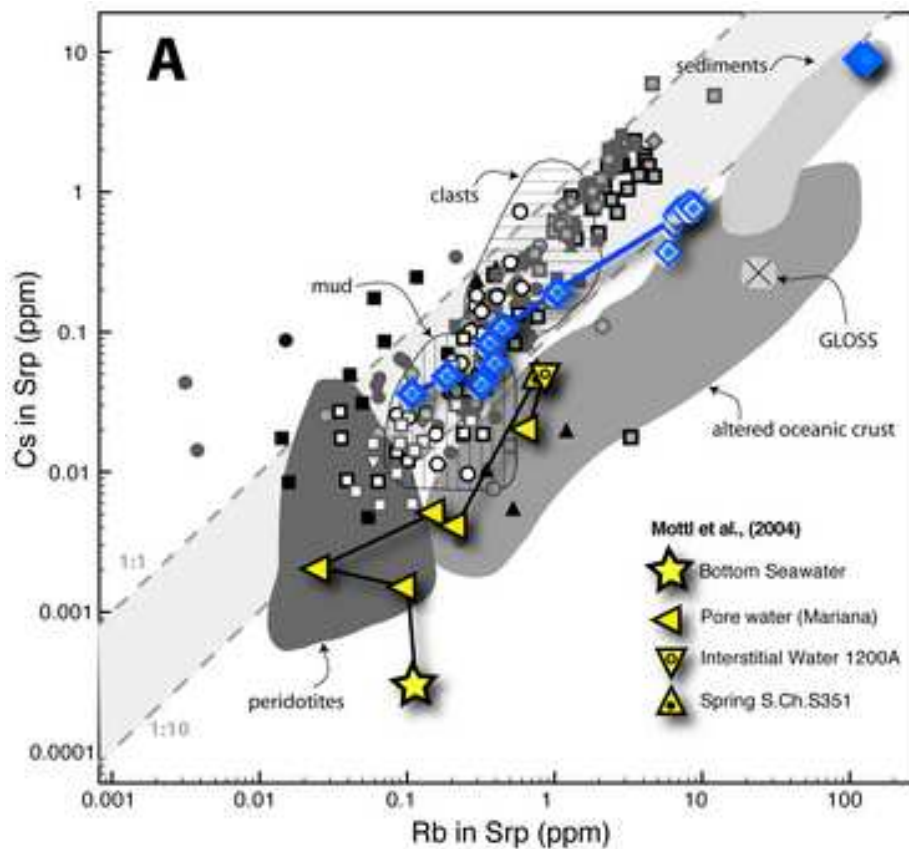
Rock-dominated system - isotropic pressure regime
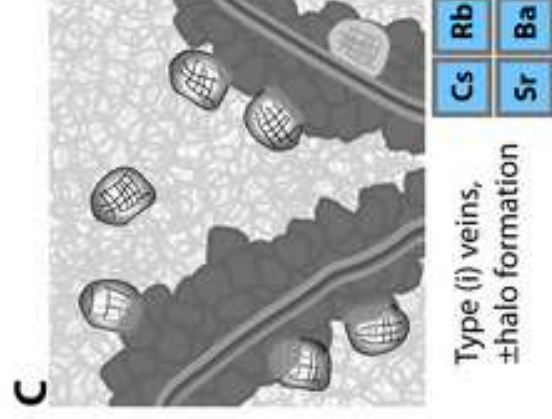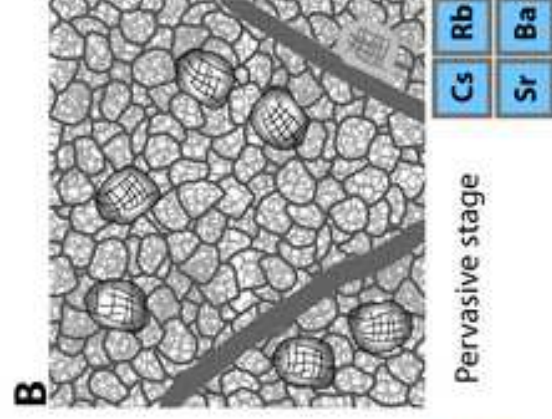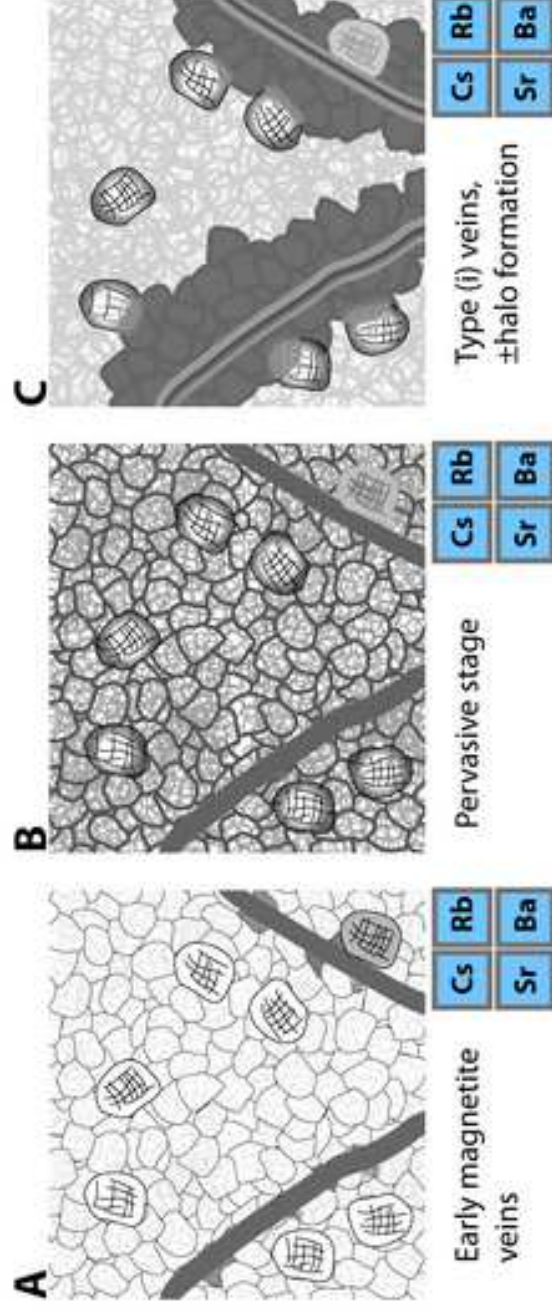
Change to fluid-dominated system - anisotropic expansion
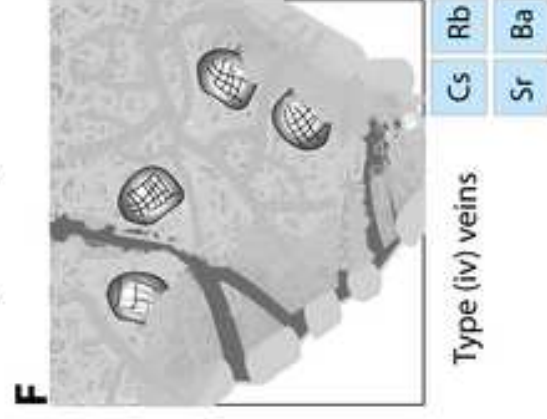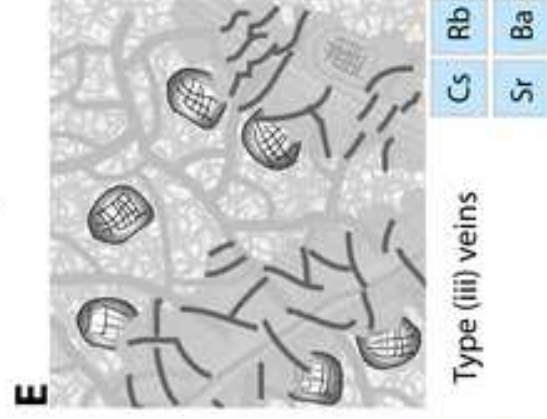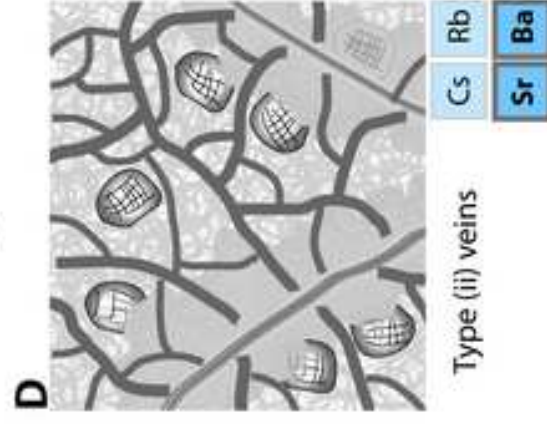
Table 1. Samples (clasts) from South Chamorro Smt., Leg 195, Site 1200A.

Sample	Short hand	Subseafloor depth (mbsf)	Rock	% alteration
near rim				
1200A-3R-1_3-7	3R-1r	18.3	Dun	99
1200A-7R-2_40-43	7R-2r	52.1	Hz	65
1200A-9R-1_21-23	9R-1r	70.6	Dun	99
1200A-10R-1_25-27	10R-1r	80.2	Hz	95
1200A-11R-1_47-49	11R-1r	89.9	Hz	100
1200A-12R-1_8-10	12R-1r	99.1	Hz	100
1200A-13R-2_5-7	13R-2r	110.0	Hz	80
1200A-16R-1_52-54	16R-1r	138.1	Hz	98
1200A-16R-2_7-9	16R-2r	139.0	Hz	70
far from rim				
1200A-3R-1_15-17	3R-1c	18.35	Hz	99
1200A-7R-2_49-51	7R-2c	52.18	Hz	70
1200A-10R-1_25-27	10R-1c	80.15	hz	97
1200A-11R-1_49-50	11R-1c	89.89	Hz	70
1200A-12R-1_13-15	12R-1c	99.13	Hz	99
1200A-13R-2_15-17	13R-2c	110.1	Hz	85
1200A-16R-1_62-64	16R-1c	138.22	Hz	95
1200A-16R-2_11-12	16R-2c	139.06	Hz	75

Table2

Table 2. Representative electron microprobe analyses and in situ LA-ICP-MS data of relict primary minerals from Leg 195, Site 1200A, South Chamorro Smt.

Sample	7R-2	16R-2	16R-1	7R-2	13R-2	16R-1	7R-2	16R-1	9R-1	16R-2
Analys. no.	27-25	22-103	94-61	6-10	28-104	20-53	17-35	7-43	156-144	5-100
Mineral	Ol	Ol	Ol	Opx	Opx	Opx	Cpx	Cpx	Spl	Spl
rock type	Hz	Hz	Hz	Hz	Hz	Hz	Hz	Hz	Dn	Hz
wt.%										
SiO2	41.12	41.27	41.38	55.63	57.07	57.27	54.65	54.12	0.02	0.02
TiO2	0.00	0.00	0.00	0.00	0.02	0.02	0.00	0.03	0.03	0.01
Al2O3	0.01	0.00	0.02	2.47	1.50	1.31	1.18	1.18	5.97	24.79
Cr2O3	0.00	0.00	0.01	1.16	0.57	0.60	0.36	0.65	55.89	43.89
FeO	8.26	7.81	8.00	5.35	5.44	5.34	2.11	1.51	18.81	19.00
MnO	0.14	0.13	0.12	0.14	0.17	0.16	0.08	0.08	0.51	0.23
MgO	50.47	51.09	50.95	32.05	35.48	34.97	19.97	17.81	7.31	12.67
CaO	0.00	0.00	0.03	3.51	0.31	0.47	21.84	24.26	0.00	0.00
Na2O	0.00	0.00	0.00	0.00	0.01	0.02	0.00	0.05	0.00	0.00
K2O	0.00	0.00	0.00	0.00	0.00	0.00	0.00	0.01	0.00	0.00
Total	100.01	100.30	100.50	100.31	100.57	100.16	100.19	99.70	88.54	100.61
Oxygens	4	4	4	6	6	6	6	6	4	4
Si	1.00	1.00	1.00	1.93	1.95	1.97	1.97	1.97	0.00	0.00
Al	0.00	0.00	0.00	0.10	0.06	0.05	0.05	0.05	0.27	0.88
Ti	0.00	0.00	0.00	0.00	0.00	0.00	0.00	0.00	0.00	0.00
Cr	0.00	0.00	0.00	0.03	0.02	0.02	0.01	0.02	1.69	1.05
Fe^{3+}*	n. c.	n. c.	n. c.	n. c.	n. c.	n. c.	n. c.	n. c.	0.03	0.06
Mg	1.83	1.84	1.83	1.66	1.81	1.79	1.07	0.97	0.42	0.57
Fe^{2+}	0.17	0.16	0.16	0.16	0.16	0.15	0.06	0.05	0.57	0.42
Mn	0.00	0.00	0.00	0.00	0.00	0.00	0.00	0.00	0.02	0.01
Ca	0.00	0.00	0.00	0.13	0.01	0.02	0.84	0.94	0.00	0.00
Na	0.00	0.00	0.00	0.00	0.00	0.00	0.00	0.00	0.00	0.00
K	0.00	0.00	0.00	0.00	0.00	0.00	0.00	0.00	0.00	0.00
Sum	3.00	3.00	3.00	4.01	4.01	4.00	4.00	4.00	3.00	2.99
Mg/(Mg+Fe2+)	0.92	0.92	0.92	0.91	0.92	0.92	0.94	0.95		
Cr/(Cr+Al)									0.86	0.54
B [µg/g]	2.5	0.2	0.1	1.3	1.4	1.1	1.0	3.9	0.5	1.6
V [µg/g]	0.5	0.4	0.4	50.9	67.9	63.2	59.1	106.5	1002	763
Ni [µg/g]	3169	3030	2983	745	663	616	386	314	188	866
Rb [µg/g]	0.0	-0.1	0.0	0.0	0.1	0.1	0.5	0.3	n. d.	n. d.
Sr [µg/g]	0.2	0.0	0.2	0.2	0.2	0.2	5.1	1.6	0.0	0.2
Cs [µg/g]	0.0	0.0	0.0	0.0	0.2	0.1	0.3	0.2	0.0	0.0
Ba [µg/g]	0.0	0.1	-0.7	0.2	0.0	0.2	0.6	0.3	0.0	0.2

Note: Hz: Harzburgite; Dn: Dunite; * calculated assuming stoichiometry; n. d.: not determined; n. c.: not calculated; b. d. l.: below detection limit.

Table 3. Representative electron microprobe analyses and in situ LA-ICP-MS data of serpentinization products from Leg 195, Site 1200A, South Chamorro Smt.

Sample	13R-2	13R-2	16R-2	16R-2	16R-2	7R-2	16R-2	16R-1	7R-2	16R-2	13R-2	3R-1	3R-1	9R-1
Analys. no.	72-126	77-128	245-132	239-63	261-50	280-49	74-83	153-37	66-40	210-125	44-114	#9-205	39-189	#8-174
Mineral	Srp	Srp-Brc	Srp	Brc	Srp-Brc	Srp-Brc	Srp	Srp-Brc	Srp-Brc	Srp	Srp	Srp	Srp	Srp
fabric type	type (i)	type (i)	type (i)-late	type (i)-late	halo (mesh)	halo (mesh)	halo (mesh)	halo (mesh)	halo (Opx)	halo (Opx)	halo (Opx)	Dn, mesh cnt.	Dn, mesh rim	Dn, recr. mesh
wt.%														
SiO2	40.86	21.24	41.45	0.51	36.42	34.87	40.04	27.47	34.04	38.08	40.87	40.16	40.73	41.00
TiO2	0.00	0.00	0.01	0.06	0.00	0.00	0.01	0.00	0.05	0.00	0.00	0.02	0.00	0.00
Al2O3	0.40	1.36	0.27	0.02	0.15	0.12	0.31	0.16	1.95	1.38	0.32	0.07	0.09	0.02
Cr2O3	0.13	0.04	0.00	0.02	0.02	0.00	0.00	0.03	0.17	0.81	0.00	0.02	0.00	0.00
FeO	5.52	8.82	5.08	42.00	5.83	6.65	4.29	6.99	6.36	6.36	4.07	3.94	4.46	2.85
MnO	0.11	0.19	0.09	0.94	0.16	0.11	0.09	0.15	0.09	0.11	0.08	0.10	0.12	0.07
MgO	37.97	41.31	38.13	32.58	38.55	39.31	38.23	39.33	37.28	34.95	37.98	37.67	38.05	39.80
CaO	0.22	0.30	0.09	0.02	0.16	0.24	0.36	0.41	0.19	0.72	0.37	0.07	0.08	0.03
Na2O	0.05	0.07	0.05	0.19	0.11	0.09	0.05	0.09	0.05	0.07	0.03	0.10	0.07	0.06
K2O	0.02	0.02	0.01	0.00	0.00	0.02	0.01	0.01	0.02	0.03	0.02	0.01	0.01	0.00
Total	85.34	73.91	85.19	76.37	81.56	81.61	83.49	74.81	81.15	82.65	83.89	82.28	83.78	83.88
Oxygens	7	7	7	2	7	7	7	7	7	7	7	7	7	7
Si	1.98	1.30	2.01	0.01	1.88	1.81	1.98	1.60	1.79	1.93	2.00	2.00	1.99	1.99
Al	0.02	0.10	0.02	0.00	0.01	0.01	0.02	0.01	0.12	0.08	0.02	0.00	0.00	0.00
Ti	0.00	0.00	0.00	0.00	0.00	0.00	0.00	0.00	0.00	0.00	0.00	0.00	0.00	0.00
Cr	0.00	0.00	0.00	0.00	0.00	0.00	0.00	0.00	0.01	0.03	0.00	0.00	0.00	0.00
Fe3+*	0.00	0.00	0.00	0.00	0.00	0.00	0.00	0.00	0.00	0.00	0.00	0.00	0.00	0.00
Mg	2.75	3.77	2.75	1.13	2.96	3.05	2.81	3.41	2.92	2.64	2.77	2.80	2.79	2.89
Fe2+	0.22	0.45	0.21	0.82	0.25	0.29	0.18	0.34	0.28	0.27	0.17	0.16	0.18	0.12
Mn	0.00	0.01	0.00	0.02	0.01	0.00	0.00	0.00	0.00	0.00	0.00	0.00	0.00	0.00
Ca	0.01	0.02	0.00	0.00	0.01	0.01	0.02	0.01	0.01	0.04	0.02	0.00	0.01	0.00
Na	0.00	0.00	0.00	0.01	0.01	0.01	0.01	0.01	0.01	0.01	0.00	0.01	0.01	0.01
K	0.00	0.00	0.00	0.00	0.00	0.00	0.00	0.00	0.00	0.00	0.00	0.00	0.00	0.00
Sum	5.01	5.66	4.99	1.99	5.12	5.19	5.02	5.40	5.15	5.01	4.99	5.00	5.00	5.01
Mg/(Mg+Fe2)	0.92	0.89	0.93	0.58	0.92	0.91	0.94	0.91	0.91	0.91	0.94	0.94	0.94	0.96
B [µg/g]	69.51	44.15	14.98	n. d.	94.50	106.01	85.59	38.62	61.71	43.65	86.87	84.54	61.13	161.41
V [µg/g]	23.55	3.79	2.15	1.82	0.70	0.62	1.17	2.26	52.47	52.92	13.25	1.41	10.17	0.97
Ni [µg/g]	1269	422	1	2	1862	1571	2137	1766	704	573	1601	3038	1867	3908
Rb [µg/g]	2.11	1.06	0.16	0.14	0.27	0.21	0.58	0.31	0.35	1.29	1.48	0.92	0.73	0.00
Sr [µg/g]	18.41	8.06	3.97	0.64	19.96	14.17	19.50	12.97	7.77	17.90	29.02	13.44	4.22	2.04
Cs [µg/g]	1.14	0.50	0.03	n. d.	0.08	0.05	0.11	0.02	0.20	0.52	0.75	0.16	0.22	b. d. l.
Ba [µg/g]	1.40	1.75	1.23	0.45	2.13	1.61	6.64	0.84	1.44	5.54	3.51	1.09	0.65	0.61

Note: Hz: Harzburgite; Dn: Dunite; * calculated assuming stoichiometry; n. d.: not determined; n. c.: not calculated; b. d. l.: below detection limit.

Table 3. Repr...

	9R-1	9R-1	16R-2	16R-2	16R-1	7R-2	13R-2	16R-2	16R-1	7R-2	7R-2	16R-1	16R-2
Sample	9R-1	9R-1	16R-2	16R-2	16R-1	7R-2	13R-2	16R-2	16R-1	7R-2	7R-2	16R-1	16R-2
Analys. no.	120-56	147-162	203-121	#24-111	137-23	#3-18	41-117	14-12	51-49	51-14	57-7	86-55	184-112
Mineral	Brc	Srp-Brc	Srp	Srp	Srp	Srp	Srp-Brc	Srp	Srp	Srp	Srp	Srp	Srp-Brc
fabric type	Dn, recr. mes†Dn, mesh rim		Hz, mesh	Hz, mesh	Hz, mesh	gran. Ol	gran. Ol	gran. Ol	Bastite	Bastite	Bastite	Bastite (Cpx)	type (ii)
wt.%													
SiO2	0.47	34.11	40.26	39.94	39.21	39.96	35.89	39.98	39.29	40.59	38.38	38.42	36.17
TiO2	0.00	0.00	0.05	0.02	0.03	0.02	0.10	0.01	0.01	0.00	0.00	0.06	0.00
Al2O3	0.03	0.01	0.10	0.13	0.21	0.64	0.00	0.02	1.23	1.79	1.72	0.65	0.03
Cr2O3			0.00	0.02	0.01	0.11	0.03	0.00	0.56	0.90	0.94	0.30	0.01
FeO	16.12	6.74	4.90	6.00	6.61	5.35	5.61	3.38	6.44	7.69	5.92	5.38	5.85
MnO	0.33	0.09	0.10	0.12	0.12	0.11	0.09	0.04	0.14	0.22	0.17	0.11	0.07
MgO	54.40	41.85	38.50	36.08	36.43	36.48	41.16	40.46	33.36	31.93	33.51	36.60	40.40
CaO	0.03	0.09	0.25	0.36	0.23	0.35	0.16	0.22	1.93	2.90	2.17	0.43	0.18
Na2O	0.05	0.04	0.07	0.04	0.05	0.06	0.01	0.03	0.05	0.12	0.13	0.03	0.07
K2O	0.02	0.00	0.03	0.04	0.00	0.03	0.00	0.04	0.02	0.05	0.02	0.03	0.01
Total	71.95	82.99	84.31	82.90	83.03	83.35	83.47	84.27	83.19	86.31	83.16	82.16	82.85
Oxygens	2	7	7	7	7	7	7	7	7	7	7	7	7
Si	0.01	1.75	1.98	2.00	1.97	1.99	1.81	1.95	1.98	1.99	1.94	1.95	1.84
Al	0.00	0.00	0.01	0.01	0.01	0.04	0.00	0.00	0.07	0.10	0.10	0.04	0.00
Ti	0.00	0.00	0.00	0.00	0.00	0.00	0.00	0.00	0.00	0.00	0.00	0.00	0.00
Cr	0.00	0.00	0.00	0.00	0.00	0.00	0.00	0.00	0.02	0.03	0.04	0.01	0.00
Fe3+*	0.00	0.00	0.00	0.00	0.00	0.00	0.00	0.00	0.00	0.00	0.00	0.00	0.00
Mg	1.69	3.20	2.82	2.70	2.73	2.71	3.10	2.94	2.51	2.33	2.53	2.77	3.06
Fe2+	0.28	0.29	0.20	0.25	0.28	0.22	0.24	0.14	0.27	0.32	0.25	0.23	0.25
Mn	0.01	0.00	0.00	0.00	0.01	0.00	0.00	0.00	0.01	0.01	0.01	0.01	0.00
Ca	0.00	0.01	0.01	0.02	0.01	0.02	0.01	0.01	0.10	0.15	0.12	0.02	0.01
Na	0.00	0.00	0.01	0.00	0.00	0.01	0.00	0.00	0.00	0.01	0.01	0.01	0.01
K		0.00	0.00	0.00	0.00	0.00	0.00	0.00	0.00	0.00	0.00	0.00	0.00
Sum	1.99	5.25	5.02	4.99	5.02	4.99	5.18	5.05	4.97	4.95	5.00	5.03	5.17
Mg/(Mg+Fe2)	0.86	0.92	0.93	0.91	0.91	0.92	0.93	0.96	0.90	0.88	0.91	0.92	0.92
B [µg/g]	n. d.	187.33	42.80	41.93	84.22	70.14	90.26	28.23	54.77	20.69	67.23	84.17	25.35
V [µg/g]	1.07	0.49	0.44	0.28	5.26	3.36	2.01	0.38	61.19	34.66	42.01	56.74	0.28
Ni [µg/g]	2431	2710	2458	2288	2534	2277	1462	2906	623	443	579	688	2154
Rb [µg/g]	0.23	0.13	3.00	2.93	0.54	2.25	2.76	2.85	3.76	3.51	3.66	2.52	0.29
Sr [µg/g]	0.32	2.34	13.77	10.81	35.43	19.32	19.99	7.68	14.36	13.62	25.09	26.85	6.66
Cs [µg/g]	n. d.	0.00	1.96	1.93	0.10	0.93	1.19	1.73	3.25	2.15	2.41	1.44	0.12
Ba [µg/g]	0.09	0.39	4.85	5.45	3.08	2.49	9.58	6.93	2.93	4.79	5.52	6.53	3.09

Note: Hz: Har

Table 3. Repr

Sample	16R-2	9R-1	7R-2	7R-2	13R-2	11R-1	16R-1	16R-1	16R-2	3R-1	3R-1
Analys. no.	185-122	#5-141	110-31	166-42	68-119	145-23	132-17	139-35	57-76	33-187	34-183
Mineral	Srp-Brc	Srp-Brc	Srp-Brc	Srp	Srp	Srp	Srp	Srp	Srp	Srp	Srp
fabric type	type (ii)	type (ii)	type (ii)	type (iii)	type (iii)	type (iii)	type (iv)	type (iv)	type (iv)	type (iv)	type (iv)
wt.%											
SiO_2	28.47	33.46	30.72	40.14	40.48	41.28	42.15	41.29	42.46	40.82	41.12
TiO_2	0.00	0.02	0.00	0.02	0.03	0.02	0.00	0.00	0.05	0.05	0.01
Al_2O_3	0.03	0.02	0.00	0.27	0.39	0.14	0.20	0.19	0.25	0.06	0.06
Cr_2O_3	0.02	0.00	0.00	0.00	0.01	0.01	0.05	0.00	0.55	0.00	0.00
FeO	7.26	6.19	6.86	5.37	8.70	5.92	5.32	5.64	4.51	3.73	4.75
MnO	0.14	0.13	0.12	0.13	0.15	0.10	0.09	0.10	0.09	0.10	0.11
MgO	43.10	42.66	42.95	38.25	35.75	38.36	38.77	38.09	38.61	38.97	38.08
CaO	0.22	0.06	0.19	0.07	0.16	0.04	0.03	0.09	0.08	0.04	0.14
Na_2O	0.07	0.09	0.01	0.06	0.09	0.02	0.01	0.04	0.03	0.04	0.07
K_2O	0.00	0.04	0.01	0.01	0.02	0.01	0.00	0.00	0.00	0.02	0.00
Total	79.37	82.66	81.01	84.39	85.86	85.92	86.65	85.48	86.65	83.89	84.48
Oxygens	7	7	7	7	7	7	7	7	7	7	7
Si	1.56	1.72	1.64	1.97	1.99	1.99	2.01	2.00	2.01	2.00	2.01
Al	0.00	0.00	0.00	0.02	0.02	0.01	0.01	0.01	0.01	0.00	0.00
Ti	0.00	0.00	0.00	0.00	0.00	0.00	0.00	0.00	0.01	0.00	0.00
Cr	0.00	0.00	0.00	0.00	0.00	0.00	0.00	0.00	0.02	0.00	0.00
$Fe^{3+}*$	0.00	0.00	0.00	0.00	0.00	0.00	0.00	0.00	0.00	0.00	0.00
Mg	3.52	3.27	3.41	2.80	2.61	2.76	2.75	2.75	2.73	2.84	2.77
Fe^{2+}	0.33	0.27	0.31	0.22	0.36	0.24	0.21	0.23	0.18	0.15	0.19
Mn	0.01	0.01	0.01	0.01	0.01	0.00	0.00	0.00	0.00	0.00	0.00
Ca	0.01	0.00	0.00	0.00	0.01	0.00	0.00	0.00	0.00	0.00	0.00
Na	0.00	0.00	0.00	0.01	0.01	0.00	0.00	0.00	0.00	0.00	0.01
K	0.00	0.00	0.00	0.00	0.00	0.00	0.00	0.00	0.00	0.00	0.00
Sum	5.44	5.28	5.37	5.02	5.01	5.01	4.99	5.00	4.97	5.00	4.99
Mg/(Mg+Fe2)	0.91	0.92	0.92	0.93	0.88	0.92	0.93	0.92	0.94	0.95	0.93
B [µg/g]	16.06	43.96	27.53	134.62	73.16	29.20	23.84	39.95	14.69	25.36	44.66
V [µg/g]	0.21	0.47	0.27	21.83	3.03	1.17	9.30	22.08	2.62	0.95	1.79
Ni [µg/g]	1872	2151	2078	43	57	7	175	193	89	71	109
Rb [µg/g]	0.11	0.08	0.17	0.33	0.53	0.11	0.11	0.24	0.09	0.16	0.34
Sr [µg/g]	4.35	3.73	9.39	1.62	9.06	0.97	2.97	9.26	2.58	0.80	1.67
Cs [µg/g]	0.06	0.01	0.07	0.05	0.08	0.01	0.01	0.07	0.01	0.02	0.03
Ba [µg/g]	2.40	0.57	1.61	0.46	1.01	0.35	0.44	1.16	0.60	0.21	0.31

Note: Hz: Har

Table 4. Overview of selected properties of serpentine from different serpentinization events.

Serpentinization phase	Schematic fabric illustration	Secondary mineralogy	Serpentine geochemistry
Early magnetite veins		Srp, Mgt	n. a.
Pervasive stage		mesh: Lz* bastite: Lz*	mesh: < 0.5 wt.% Al_2O_3 in Srp; bastite: up to 2.4 wt.% Al_2O_3; Mesh: low V, high Ni; bastite: high V, low Ni; **Cs, Rb, Sr, Ba**
Type (i) veins		Liz*, Brc	up to 2.0 wt.% Al_2O_3; **Cs, Rb, Sr, Ba**
Type (ii) veins		Ctl*, Brc	up to 0.9 wt.% Al_2O_3; low V, high Ni; Cs, Rb, **Sr, Ba**
Type (iii) veins *"Frankenstein"*		Ctl*	up to 1.0 wt.% Al_2O_3; V, low Ni; Cs, Rb, Sr, Ba
Type (iv) veins *multiple crack-seal*		Ctl*	up to 0.8 wt.% Al_2O_3; V, low Ni; Cs, Rb, Sr, Ba

Note: n. a. not analyzed; *confirmed by micro-Raman; trace element contents: **bold**-relatively high values, plain-relatively low values.

Table 5. Oxygen isotope data of serpentinization products from different serpentinization phases in ultramafic clasts from South Chamorro Smt., Leg 195, Site 1200A.

Sample	% serp	fabric type	minerals #	$\delta_{18}O*$
3R-1, 3-7 cm	100	type (iv) vein	Ctl	6.9
7R-2, 40-43 cm	97	halo region around type (i) vein	Liz, Ctl	7.6
10R-1_54-62 cm	100	vein, type (iv)	Ctl	6.4; 6.1
11R-1, 47-49 cm	100	vein in clast brown rim zone	Ctl	6.4
12R-1, 8-11 cm	100	bastite in brown clast rim zone	Ctl; Palyg, Sep, Sap (15 vol.%)	8.1
13R-2, 5-7 cm	100	chrysotile vein, type (iv)	Ctl	10.5
13R-2, 5-7 cm	100	serpentine, type (ii)		7.3
16R-2, 7-9 cm	97	type (ii) veins	Ctl, Liz, Brc (13 vol.%)	7.3
16R-2, 7-9 cm	97	type (i)/ reactivated by type (iv) vein	Liz, Ctl, Brc (4 vol.%)	6.6

Note: #determined by XRD; * VSMOW.